INP/INAS QUANTUM WELL INFRARED PHOTODETECTORS

A THESIS SUBMITTED TO
THE GRADUATE SCHOOL OF NATURAL AND APPLIED SCIENCES
OF
MIDDLE EAST TECHNICAL UNIVERSITY

BY

OĞUZ ONUR GÜNGÖR

IN PARTIAL FULFILLMENT OF THE REQUIREMENTS
FOR
THE DEGREE OF MASTER OF SCIENCE
IN
ELECTRICAL AND ELECTRONIC ENGINEERING

SEPTEMBER 2023

Approval of the thesis:

INP/INAS QUANTUM WELL INFRARED PHOTODETECTORS

submitted by **Oğuz Onur Güngör** in partial fulfillment of the requirements for the degree of **Master of Science in Electrical and Electronic Engineering, Middle East Technical University** by,

Prof. Dr. Halil Kalıpçılar
Dean, Graduate School of **Natural and Applied Sciences** _____

Prof. Dr. İlkay Ulusoy
Head of the Department, **Electrical and Electronics Engineering** _____

Prof. Dr. Cengiz Beşikci
Supervisor, **Electrical and Electronics Engineering, METU** _____

Examining Committee Members:

Prof. Dr. Barış Bayram
Electrical and Electronics Engineering, METU _____

Prof. Dr. Cengiz Beşikci
Electrical and Electronics Engineering, METU _____

Doç. Dr. Dinçer Gökcen
Electrical and Electronics Engineering, Hacettepe University _____

Date: 08.09.2023

I hereby declare that all information in this document has been obtained and presented in accordance with academic rules and ethical conduct. I also declare that, as required by these rules and conduct, I have fully cited and referenced all material and results that are not original to this work.

Name Last name : Oğuz Onur Güngör

Signature :

ABSTRACT

INP/INAS QUANTUM WELL INFRARED PHOTODETECTORS

Güngör, Oğuz Onur
Master of Science, Electrical and Electronic Engineering
Supervisor : Prof. Dr. Cengiz Beşikci

September 2023, 79 pages

Quantum well infrared photodetectors (QWIPs) are advantageous regarding detector uniformity, stability, and cost compared to other infrared detector technologies. On the other hand, they suffer from low quantum efficiency (QE) because they cannot detect normal-incidence radiation. Diffraction-gratings and special mesa structures are used to increase QE by manipulating the incoming radiation. These solutions complicate the detector production process and increase the crosstalk between pixels. Also, they lose their effectiveness when the pixel size is reduced to have a higher resolution and lower cost. Recent studies on new material systems to increase QE give promising results even without diffraction-gratings and special mesa structures. This thesis presents grating-free mid-wavelength QWIPs with high conversion efficiency (CE) based on the InP/InAs material system on InP substrate.

Molecular beam epitaxy grown epilayer of the detectors consisted of InP barriers and Si-doped InAs quantum wells. A diffraction-grating-free focal plane array (FPA) with 15 μm pitch and 640x512 format and individual pixel arrays were fabricated and characterized. The cut-off and peak responsivity wavelengths of the pixels were 6.2 and 5.5 μm, respectively. Responsivity measurements exhibited a

peak responsivity as high as 2.7 A/W under -4.0 V bias voltage, corresponding to a peak CE of 61%. The mean noise equivalent temperature difference (NETD) of the FPA was approximately 28 mK with f/1.67 optics at 10 ms integration time, which is consistent with the calculated NETD based on the measurements on pixel arrays. These results show that QWIPs based on properly chosen alternative material systems are indispensable alternatives to HgCdTe and Type-II superlattice detectors.

Keywords: Quantum Well Infrared Photodetector, Mid Wave Infrared, Infrared Detector

ÖZ

INP/INAS KUANTUM KUYULU KIZILÖTESİ FOTODEDEKTÖRLER

Güngör, Oğuz Onur
Yüksek Lisans, Elektrik ve Elektronik Mühendisliği
Tez Yöneticisi: Prof. Dr. Cengiz Beşikci

Eylül 2023, 79 sayfa

Kuantum kuyulu kızılötesi fotodedektörler (KKKF), diğer kızılötesi dedektör teknolojilerine kıyasla dedektör homojenlik düzeyi, kararlılığı ve maliyeti açısından avantajlıdır. Öte yandan, dedektör yüzeyine dik gelen radyasyonu algılayamadıkları için düşük kuantum verimliliğinden muzdariptirler. Kuantum verimliliğini artırmak için gelen radyasyonun yönünü değiştiren optik ızgaralar ve özel mesa yapıları kullanılmaktadır. Bu çözümler, dedektör üretim sürecini karmaşıklaştırmakta ve bitişik pikseller arasındaki etkileşimi arttırmaktadır. Ayrıca, daha yüksek çözünürlük ve daha düşük maliyet için piksel boyutu küçültüldüğünde, etkinliklerini de kaybederler. Kuantum verimliliğini artırmak için yeni malzeme sistemleri geliştirmeye yönelik son çalışmalar, kırınım ızgaraları ve özel mesa yapıları kullanmamalarına rağmen, umut verici sonuçlar vermiştir. Bu tez, InP taban üzerine büyütülen InP/InAs malzeme sistemine dayanan, yüksek çevirim verimliliğine sahip, kırınım ızgarasız orta dalga boyuna duyarlı KKKF'leri raporlamaktadır.

Molecular Beam Epitaxy sistemi kullanılarak büyütülen dedektörlerin epi katmanı, InP bariyerlerden ve Si katkılı InAs kuantum kuyularından oluşmaktadır. 15 μm dedektör adımına sahip 640x512 formatında odak düzlemi dizini (ODD) ve ayrık

piksel dizinleri üretilmiş ve karakterize edilmiştir. Dedektörün üst kesim ve tepe duyarlılık dalga boyları yaklaşık 6.2 ve 5.5 μm'dir. Duyarlılık -4.0 V gerilim voltajı altında 2.7 A/W olacak kadar yüksek olup %61'lik tepe çevirim verimliliğine karşılık gelmektedir. ODD'nin gürültü eşdeğer sıcaklık farkı (GESF), f/1.67 optik ve 10 ms entegrasyon zamanıyla, 28 mK olarak ölçülmüş olup, piksel dizinlerinden hesaplanan GESF değeri ile uyumludur. Elde edilen sonuçlar, doğru bir şekilde seçilen alternatif malzeme sistemlerine dayanan KKKF'lerin HgCdTe ve Tip-II süperörgü dedektölere karşı hala vazgeçilmez alternatifler olduğunu göstermiştir.

Anahtar Kelimeler: Kuantum Kuyulu Kızılötesi Fotodedektör, Orta Dalga Boylu Kızılötesi, Kızılötesi Dedektör

To my Family

ACKNOWLEDGMENTS

First and foremost, I would like to thank my supervisor, Prof. Dr. Cengiz Beşikci, for his help, guidance, and advice in every step of my thesis studies, from the material growth to the measurements of the detector. I also thank him for giving me the opportunity to work in KANAL.

I want to thank Assoc. Prof. Serdar Kocaman for his support and valuable feedback during my KANAL days.

I want to thank Prof. Dr. Barış Bayram and Assoc. Dr. Dinçer Gökcen for being on my thesis committee.

I would also like to give special thanks to my heartfelt friend and companion, Saadettin Veysel Balcı, for all the help in the fabrication process of the detectors and for the best friendship throughout my thesis study.

I want to thank Onur Tanış for the characterization of the produced FPA and the friendship during my graduate study.

I would like to thank Onur Tanış, Musa Selim Gül, Alper Şahin, Kübra Çırçır, Halil İbrahim Binici, and Necati Işık for their friendship and support.

The technical assistance of Transvaro Elektron Aletleri San. Tic. Aş. is gratefully acknowledged. In addition, I would like to thank Mr. Akın Aydemir, Mr. İsmail Eken, Ms. Bengisu Sayın, and Mr. Berkay Uğurlu during the indium coating and flip-chip bonding of the detectors.

I would also like to thank Özgür Necip Şen for his best efforts and patience in the administrative works of our laboratory.

Last but not least, I would like to thank my family for their endless and generous support throughout my academic career, from primary school to this day.

TABLE OF CONTENTS

LIST OF TABLES

TABLES

LIST OF FIGURES

FIGURES

CHAPTER 1

INTRODUCTION

In general, the human eye cannot see infrared (IR) radiation; special devices called detectors are needed to see it. For more than a century, scientists worldwide have continued to develop proper detectors to sense IR radiation. Currently, numerous commercially available detectors are sensitive to infrared radiation in either a single or multiple wavelength band(s). Thanks to advancements in semiconductor technology over the last century, these detectors are now more affordable and accessible. While initially developed for military purposes, they are now utilized in critical fields such as weather forecasting, firefighting, astronomy, and medicine.

Today, the most widely studied IR detector technologies are Mercury Cadmium Telluride (HgCdTe) photodiodes, Microbolometers, and Type-II Superlattices (T2SLs). Even though HgCdTe technology provides the highest quantum efficiency (QE), its growth with high crystalline quality is expensive and challenging [1]. Microbolometers are much cheaper but slow and have low sensitivity [2]. Type-II Superlattices are currently a hot topic in the area. Although T2SL detectors with good characteristics are already produced, they have optical crosstalk and limited diffusion length problems [3].

Quantum well infrared photodetectors (QWIPs) represent another critical IR detector technology. They have high uniformity, operability, reproducibility, thermal cycling stability, and temporal coherence. Also, they have zero 1/f noise, unlike HgCdTe and T2SLs. The main disadvantage of the GaAs-based standard QWIPs is low quantum efficiency compared to other technologies [4]. This is because they cannot detect the normal incidence radiation. Still, they are widely used for thermal imaging with the help of diffraction-gratings or special mesa

structures [5-6]. Scientists working on standard QWIP technology aim to get smaller pixels and have multispectral/polarimetric imaging [7-8].

Two critical requirements of the third-generation infrared photodetectors are small pixel pitch and dual/multi-band detection capability [9]. Dual-band HgCdTe, T2SL, and QWIP detectors are commercially available now with some limitations. Because of their wide spectral response, HgCdTe and T2SL suffer from optical crosstalk [3]. HgCdTe detectors also require thick absorber layers for sufficient QE [10-11]. Thick epilayers make the etching process difficult, especially for dual-band applications. T2SL detectors also need thick absorbers or barrier layers to lower optical crosstalk between spectral windows [10]. Standard QWIPs, on the other hand, do not need thick absorber layers, and their inherently narrow spectral response eliminates the optical crosstalk. The problem with the standard QWIP technology is the diffraction-grating requirement. Gratings lose their efficiency for small pixel pitches, especially for the mid-wavelength IR (MWIR) band [4].

Scientists continue to work on alternative material systems for QWIPs to increase QE with normal incidence radiation. For example, it is experimentally proven that InGaAs/GaAs QWIPs can detect normal incidence radiation [12-13]. However, the QE of these detectors still needed to be higher to compete with other technologies. Other examples can be the p-type (p-doped) AlGaAs/GaAs [14] and the strained InGaAs/GaAs [15] material systems. Last but not least, MWIR InP/InGaAs QWIPs on InP substrate were studied experimentally and theoretically by Besikci *et al.* [16]. Results show that they have high photoconductive gain under large bias and moderately high QE, resulting in enough conversion efficiency to eliminate gratings. As a continuation of this work, this thesis introduces MWIR QWIPs with binary InP/InAs material system as a new alternative.

The first chapter of this thesis discusses the basics of IR radiation and the laws governing the events in the field. Then, IR detector types and figures of merits are discussed briefly. In the next chapter, QWIP technology and the current state of the art are presented in detail. The third chapter demonstrates the implementation and

characterization results of the proposed MWIR QWIPs. In the last chapter, the overall work is summarized, and possible future studies are discussed.

1.1 Infrared Radiation Fundamentals

All objects above 0 K emit electromagnetic radiation (or photons) in different wavelengths. It is called thermal radiation and, in theory, covers the entire electromagnetic spectrum. The reason for this self-radiation is the molecular excitations that cause transitions in the material [17]. The temperature of an object dictates the wavelength range at which most of the emission occurs. In the case of objects in our surroundings, this range falls within the electromagnetic spectrum's infrared (IR) region. As a result, detecting IR radiation is a vital area of research.

In addition to self-emission, matters can absorb, transmit, or reflect some parts of the thermal radiation falling on them. Considering the conservation of energy, the relation between these three events can be written as

$$\alpha + \rho + T = 1 \qquad (1.1)$$

where α (absorbance) is the ratio of absorbed energy to total incident energy, ρ (reflectance) is the ratio of reflected energy to total incident energy, and T (transmittance) is the ratio of transmitted energy to total incident energy [17]. When the absorbance of an arbitrary object is equal to 1 ($\rho = T = 0$) for all wavelengths, it is called a Blackbody (BB). As the name implies, BBs absorb all the incoming radiation regardless of wavelength. They are the ideal emitters since they emit all the absorbed energy.

The emission of all the absorbed energy is the common property of all objects at thermodynamic equilibrium. It is known as Kirchhoff's Law of Thermal Radiation and is written as [17]

$$\alpha = \varepsilon \qquad (1.2)$$

In Equation 1.2, ε is the object's emissivity and is described as the ratio of the object's actual exitance to the exitance of a BB at the same temperature. For BBs, it is wavelength-independent and equal to 1. However, it is wavelength-dependent for the everyday objects around us and less than 1. In addition, if the emissivity of an object is less than one and still wavelength-independent, it is called a greybody.

Spectral radiant exitance is the amount of power per unit area per unit wavelength emitted from a body for a given temperature and wavelength. For BBs, it can be calculated using Planck's Law

$$M_\lambda(T) = \frac{2\pi hc^2}{\lambda^5\left(e^{\frac{hc}{\lambda kT}} - 1\right)} \quad (1.3)$$

where c is the speed of light, h is Planck's constant, k is the Boltzmann constant, and T is the temperature of the BB [17]. Integrating $M_\lambda(T)$ over a wavelength range would give the total exitance per unit area of the BB over that range. For example, a BB's spectral radiant exitance for different temperatures is shown in Figure 1.1.

As seen in Figure 1.1, the exitance peak of the hot objects is around the visible spectrum (0.4 μm to 0.7 μm). Thus, the human eye can detect radiation emitted by hot objects such as the sun, which has a surface temperature of around 6000 K. However, the peak of the near room temperature objects (300 K) occurs around 10 μm.

Planck's Law can also be described in terms of the number of photons per unit area per second per unit wavelength by dividing Equation 1.3 by the energy of a single photon (hc/λ). It is named spectral photon exitance and can be written as

$$M_p(T) = \frac{2\pi c}{\lambda^4\left(e^{\frac{hc}{\lambda kT}} - 1\right)} \quad (1.4)$$

where c is the speed of light, h is Planck's constant, k is the Boltzmann constant, and T is the temperature of the BB [17]. Integrating $M_p(T)$ over a wavelength range would give the total number of photons per unit area per second of the BB over that range.

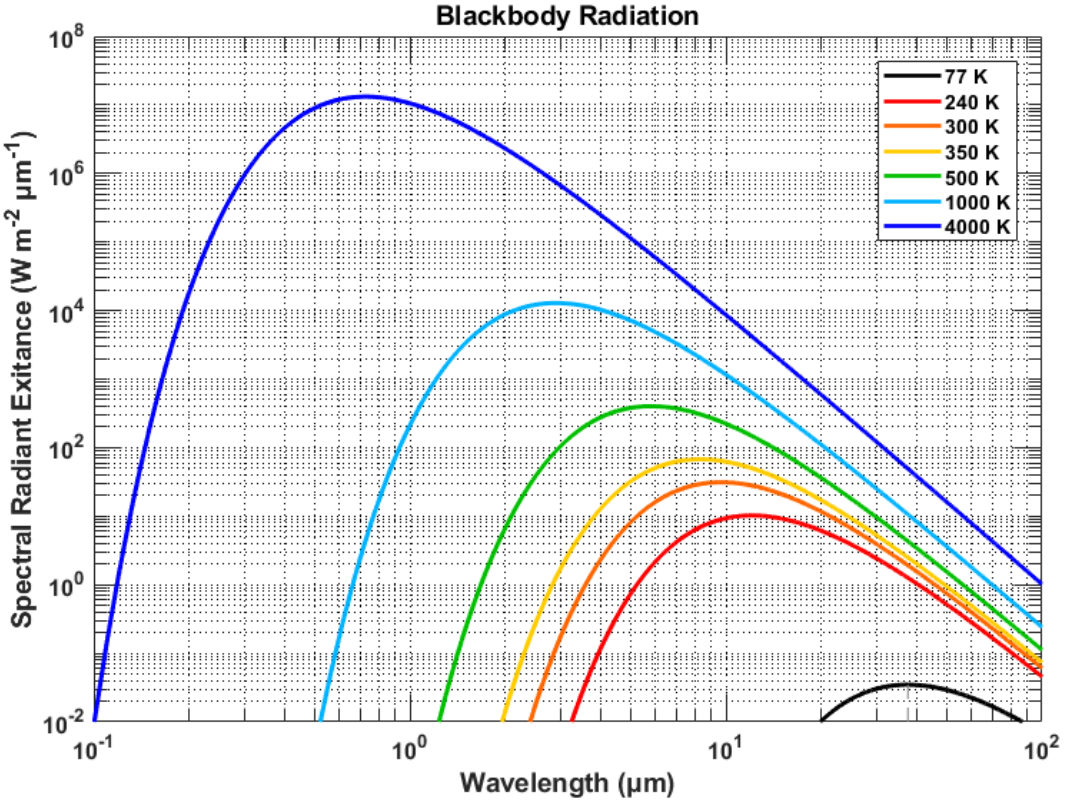

Figure 1.1: Blackbody spectral radiant exitance for different temperatures.

There is an easier way to calculate the wavelength at which the exitance of the BB peaks for a given temperature. From a mathematical point of view, equating the derivative of $M_\lambda(T)$ with respect to λ to 0 and solving for λ gives the peak wavelength. This is also known as Wien's Displacement Law and is written as

$$\lambda_{max} = \frac{2898\ \mu m.K}{T} \qquad (1.5)$$

where T is the temperature in K [17]. For $T = 300\ K$, it is around 10 μm and, for $T = 6000\ K$, it is around 0.5 μm.

As stated previously, for emissivity calculation, the total exitance from a BB must be known at a given temperature. It can be done by integrating $M_\lambda(T)$ or $M_p(T)$ from $\lambda = 0$ to $\lambda = \infty$. This calculation results in Stefan-Boltzmann Law for $M(T)$:

$$M(total) = \sigma T^4 \tag{1.6}$$

where σ is the Stefan-Boltzmann constant and equals 5.67032×10^{-12} W/cm^2-K^4 [17]. For example, the average human body with a 2 m^2 area, 305 K temperature, and near unity emissivity has a total exitance power of around 1000 W [17].

For thermal imaging applications, how well the target object can be distinguished from the background is an essential detector performance parameter. It depends on the thermal contrast of the detector and changes with the wavelength interval to which the detector is sensitive. The equation for the thermal contrast is [17]

$$Contrast = \frac{\int_{\Delta\lambda} M_\lambda(\lambda, T_{obj})\, d\lambda - \int_{\Delta\lambda} M_\lambda(\lambda, T_{back})\, d\lambda}{\int_{\Delta\lambda} M_\lambda(\lambda, T_{obj})\, d\lambda + \int_{\Delta\lambda} M_\lambda(\lambda, T_{back})\, d\lambda} \tag{1.7}$$

where T_{obj} is the target object temperature, T_{back} is the background temperature, and $\Delta\lambda$ is the wavelength interval. Example contrast values for different object temperatures and wavelength intervals are shown in Figure 1.2 [17]. It is evident from Figure 1.2 that thermal contrast increases with decreasing wavelength and background temperatures. Thus, the 3.5-5 μm range is better than the 8-14 μm range in terms of thermal contrast.

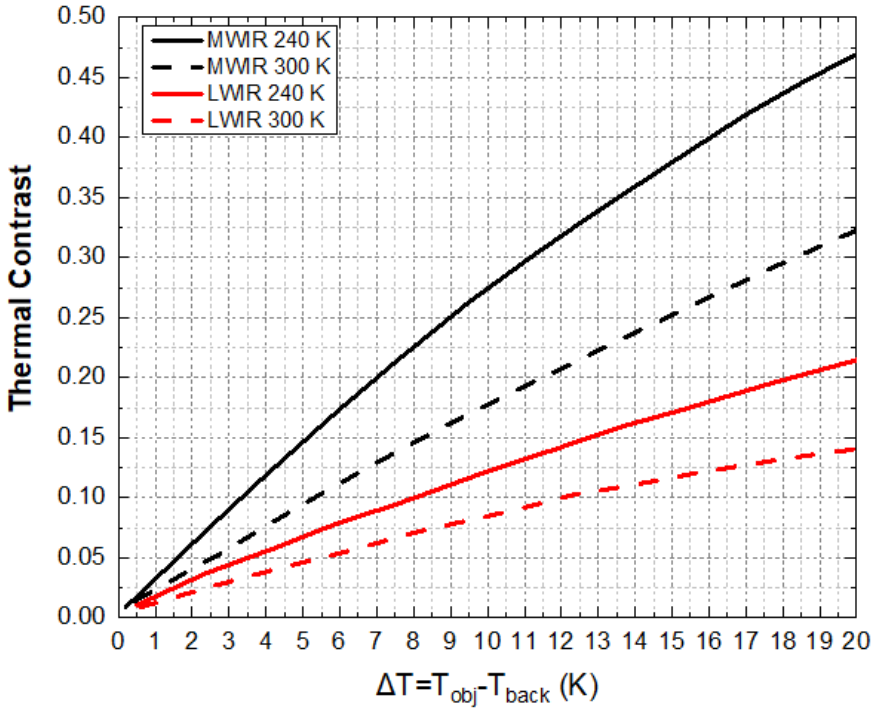

Figure 1.2: Thermal contrasts in wavelength intervals 3.5-5 μm (MWIR) and 8-14 μm (LWIR) (redrawn after [17]).

1.2 Transmission of the Infrared Radiation

In most IR detector applications, the medium for the IR radiation between the source and the detector is the atmosphere of Earth. During its travel, radiation emitted from the source will be attenuated before reaching the detectors because of the atmospheric gasses' absorption and the particles' scattering. They must be taken into account during the design of the detector since the amount of radiation arriving at the detector will be considerably smaller than the radiation emitted from the source. The radiation's absorption and scattering amounts change depending on the medium's content and density. They also depend on the wavelength of the photons.

Even if the radiation arrives at the detector, some of the radiation is still lost because of the reflection from the detector's surface. However, anti-reflection coatings (AR) can minimize these losses.

Atmospheric gasses like H_2O, CO_2, O_3, CO, CH_4, and N_2 are responsible for the absorption of IR radiation because of the vibrational states of their atoms [17]. Radiation going through these gases attenuates exponentially with the distance traveled. Dominant ones are H_2O and CO_2. As an example, the former absorbs most IR radiation within the wavelength range of 5.5-7.5 μm, even at relatively short distances [17]. The latter attenuates the IR radiation almost entirely in the 4.2-4.4 μm and 2.6-2.9 μm ranges [17].

While traveling, IR radiation scatters because of the particles in the air, such as atmospheric molecules and aerosols. The former ones have sizes smaller than the radiation wavelength. Examples can be CO_2, O_3, and N_2 [17]. This type of scattering is called Rayleigh Scattering. It is also the reason why the sky is blue. On the other hand, the latter ones are larger than the radiation wavelength. Examples of this category include fog, smoke, and dust [17]. This type of scattering is called Mie Scattering.

Absorption and scattering of the radiation are represented with wavelength-dependent parameters for each molecule or particle. The amount of transmittance after absorption and scattering can be calculated mathematically using the formula:

$$T(\lambda) = e^{-(K_a+\gamma)x} \quad (1.8)$$

where K_a is the absorption coefficient, γ is the scattering coefficient, and x is the distance radiation travels before reaching the detector [17]. Experimental measurements and physics principles are used to find the coefficients for each molecule or particle. After finding the transmittance values for each factor, overall transmittance is found by multiplying them as follows [17]

$$T_{overall}(\lambda) = T_{factor\,1}(\lambda).T_{factor\,2}(\lambda).T_{factor\,3}(\lambda).\ldots \quad (1.9).$$

When all of the attenuation factors are put together, the transmission spectrum of the atmosphere is obtained. It is shown in Figure 1.3 for a distance of approximately 1.85 km [18].

As seen in Figure 1.3, the atmosphere is transparent to IR radiation only at some wavelength ranges, which are called atmospheric windows. IR region of the electromagnetic spectrum is divided into subcategories given in Table 1.1, considering the atmospheric windows. The number and borders of these regions are still in discussion. For instance, the SWIR region is sometimes split into SWIR (1-1.7 μm) and Extended-SWIR (2-2.5 μm).

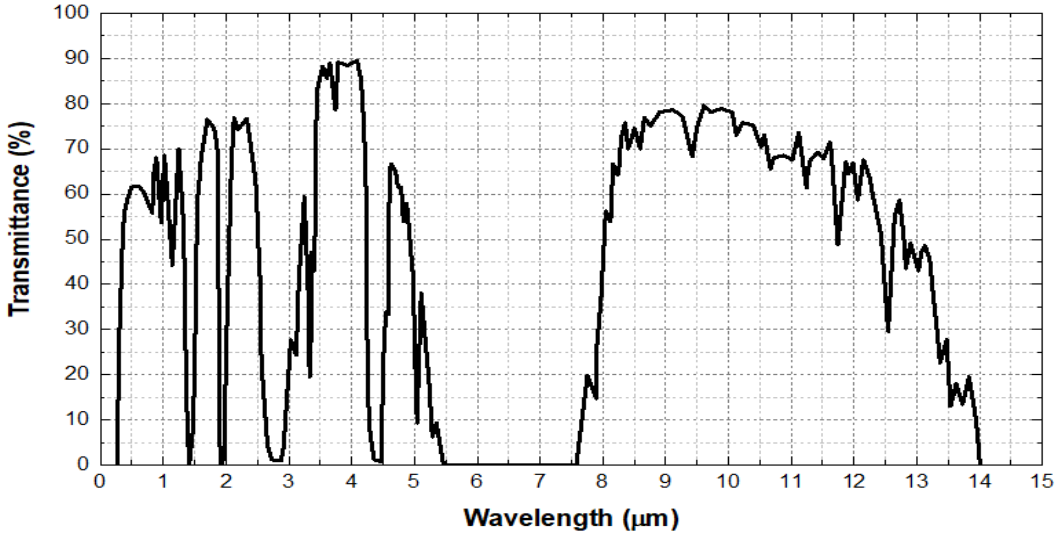

Figure 1.3: Transmission spectrum of the atmosphere in the infrared region (redrawn after [18]).

Table 1.1: IR region of the electromagnetic spectrum.

Subcategory Name	Abbreviation	Wavelength Range (μm)
Short Wave IR	SWIR	1-3
Mid Wave IR	MWIR	3-5
Long Wave IR	LWIR	8-14
Very Long Wave IR	VLWIR	14-30
Far IR	FIR	20-1000

Each of these wavelength bands has distinctive properties and application areas. For example, the MWIR band is preferred over the LWIR band in terms of thermal contrast, as shown in Figure 1.2. The LWIR band, on the other hand, is advantageous in terms of higher received photon flux from near room temperature objects. The SWIR region is the best option in terms of resolution, but the photon flux of near room temperature objects is low in this region. SWIR detectors are used for night vision and long-range fiber optic communication. The VLWIR and FIR regions are used to detect radiation coming from relatively cold objects like interstellar gases. Thus, they are frequently used in astronomy.

1.3 Infrared Detectors

According to the operation principle, infrared detectors can be classified as thermal and photon detectors. Each of these categories will be discussed separately.

1.3.1. Thermal Detectors

Absorption of the radiation can increase the temperature of the material absorbing it. Temperature changes can further change the material's properties, such as size, resistance, or electrical polarization. Thermal detectors utilize these changes to sense IR radiation and convert it into electrical signals with a proper electrical circuit.

Significant advantages of thermal detectors are lower cost and no requirement for cooling. Major disadvantages, on the other hand, are the lower signal-to-noise ratio (SNR) and higher response time [19]. Since the detection is done via temperature change and the detector is in contact with its surroundings, heat exchange between the detector and its environment creates fluctuations in the detector temperature. This, in return, creates an additional temperature fluctuation noise and lowers the SNR of the detector. Additionally, the thermal detectors' response time is higher

(in the order of milliseconds) because the heating and cooling of the detectors cannot happen instantaneously [19].

One of the most common thermal detector types is the microbolometer [19]. They utilize the change in the detector material's resistance with the temperature difference. Vanadium oxide and amorphous-Si are the most widely used absorber materials for microbolometers [20].

Another type of thermal detector is thermoelectric arrays, which employ the Seeback Effect. A potential difference is observed when there is a temperature difference between two junctions with different Seeback coefficients. They are called thermocouples. Because of this internal voltage creation property, they do not require a biasing voltage. In addition, this eliminates any 1/f noise and bias-induced heating [20]. However, their responsivity is low, and the large pixel size requirement makes the production of large-format FPAs difficult [20].

Pyroelectric array is another type of thermal detector exhibiting an internal electrical polarization as a response to temperature change. This polarization change is detected as a voltage difference at the output of the detector.

Current research on thermal detectors focuses on reducing pixel size to increase resolution and decrease cost [20].

1.3.2. Photon Detectors

The other type of IR detectors is photon detectors. As the name implies, they are sensitive to individual photons and have a wavelength-dependent responsivity spectrum. Photons are absorbed by the material’s carriers (electrons or holes). These carriers taking the energy of the absorbed photons are excited to an allowed higher energy state in the material. Then, excited carriers create a current with the help of either a bias voltage or a built-in E-field. The former ones are photoconductive, and the latter ones are photovoltaic photon detectors.

According to the initial energy level of the carrier, photon detectors can also be divided into intrinsic and extrinsic photon detectors. In the first one, carriers move from the valence band to the conduction band or vice versa. This type of excitation is called interband excitation or direct generation. In the second type, on the other hand, carriers located between the valence band and the conduction band move to either the valence or conduction band. Impurities are intentionally added to the material to create carriers in the forbidden bandgap of the intrinsic material. Additionally, another type of excitation can occur both in intrinsic and extrinsic materials. Confinement of the carriers to discrete energy levels with special quantum structures will create subbands in the valence and conduction band of the material. They are called intersubband transitions.

The main advantages of photon detectors over thermal ones are their low response time and high SNRs. The response time of the photon detectors is in the order of picoseconds since photon interactions happen almost instantaneously [19]. Thus, high frame rates with low integration time are possible. Additionally, because they are operated under low and stable temperatures, their noise signals are low, resulting in high detectivity.

The relation between photon energy and its wavelength is given as [17]

$$E_p(\lambda) = \frac{1.24}{\lambda\ (\mu m)}\ eV \qquad (1.10).$$

This energy is small for commonly used IR regions (MWIR and LWIR) (around 0.31 and 0.14 eV, respectively). Thus, materials with low bandgap or small energy intersubband transitions are needed to detect IR.

Today's most widely used IR photon detectors can be categorized into two families: quantum-structured IR photodetectors (QSIPs) and low bandgap materials. Quantum well IR photodetectors (QWIPs), quantum dot IR photodetectors (QDIPs), and Type-II superlattices (T2SLs) are widely studied examples of the

QSIP family. For low bandgap materials, HgCdTe and InSb can be given as examples.

InSb

InSb is a low-bandgap photoconductive material with a fixed bandgap energy of 0.224 eV. This energy level corresponds to a cut-off wavelength of 5.5 μm. Therefore, it is used only as MWIR detector material. This makes its application area limited. Dual-band sensors are not possible as a natural result of this drawback.

HgCdTe

With its adjustable bandgap energy, the 1-25 μm range of the IR spectrum can be covered with HgCdTe IR detectors. The bandgap of the HgCdTe can be adjusted easily by changing the Cd mole fraction. Advantageously, as shown in Figure 1.4, the lattice constant remains almost fixed with the Cd mole fraction change [21]. Figure 1.4 also shows the bandgap of the HgCdTe at two different temperatures with changing CdTe (or Cd) mole fraction.

QWIPs

As a member of the QSIP family, Quantum Well Infrared Photodetectors (QWIPs) are formed by growing low and large bandgap materials one after the other. Figure 1.5 [22] shows that the bandgap difference creates discontinuities (wells) in the valence and conduction bands. Large and low bandgap materials are called barrier and well, respectively. Confinement of the carriers in the well creates discrete energy levels for carriers to occupy. The first level in Figure 1.5 is called the ground state. Exciting the carriers to a higher energy level above the conduction band or below the valence band edges of the barrier material makes the carriers free for conduction. Collecting the excited carriers by applying a bias voltage produces a current.

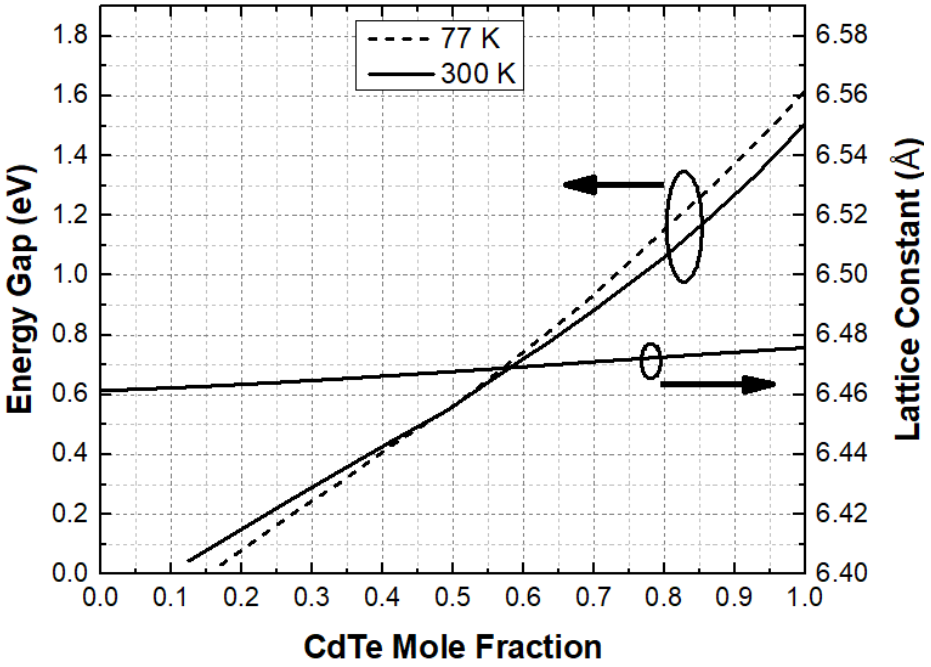

Figure 1.4: Lattice constant and bandgap energy of HgCdTe for different Cd mole fractions (redrawn after [21]).

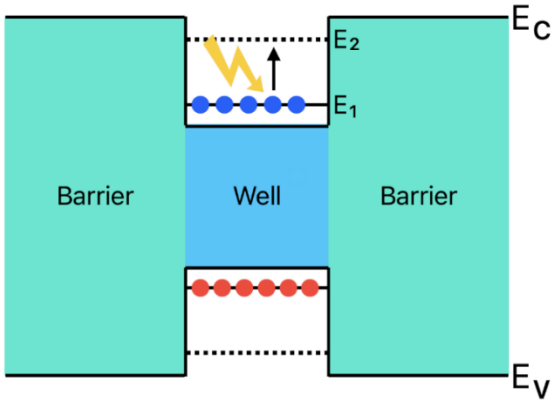

Figure 1.5: Intersubband transitions occurring in quantum wells (redrawn after [22]).

Mature material systems for MWIR QWIPs are AlGaAs/InGaAs and AlInAs/InGaAs. For the LWIR band, AlGaAs/GaAs is the standard material system.

Since it is related to the topic of this thesis, this technology will be discussed in the next chapter in detail.

QDIPs

Quantum Dot Infrared Photodetectors (QDIPs) were initially designed as an alternative to the QWIP technology. Rather than confining the carriers in 1 dimension, in QDIPs, they are confined in all 3-dimensions. Theoretically, they were expected to provide higher quantum efficiency and photoconductive gain than QWIPs [76]. However, this technology has been almost abandoned because of the difficulties like dot size nonuniformity throughout the device and residual strain [76].

T2SLs

Type-II Superlattice (T2SLs) technology is currently the most frequently studied IR detector technology. Like QWIPs and QDIPs, alternating low and large bandgap materials are used to create minibands, as shown in Figure 1.6 [23]. Good performance results with high QE comparable with HgCdTe are already available, especially in the MWIR band [23]. InAs/GaInSb and InAs/GaSb on GaSb substrates are examples of high-performance T2SL material systems [23,24].

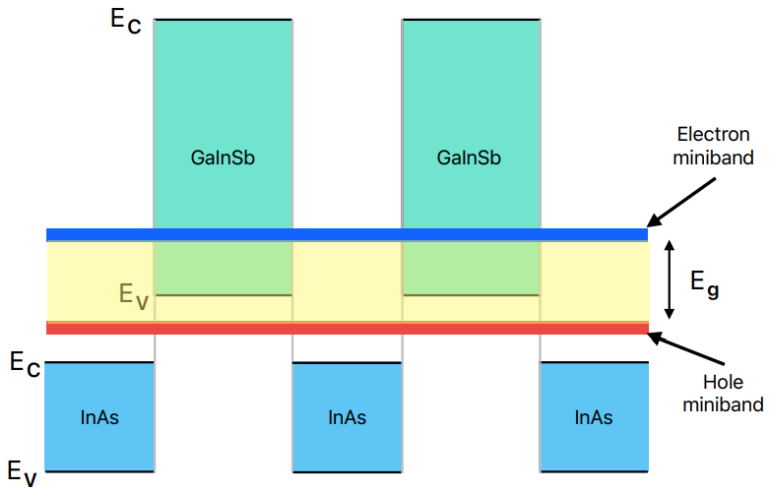

Figure 1.6: Band diagram of InAs/GaInSb Type-II Superlattice structure (redrawn after [23]).

1.4. Figure of Merits for Infrared Detectors

Performance comparison parameters for IR detectors are responsivity, noise sources and amounts, noise equivalent power, detectivity, and noise equivalent temperature difference. As described previously, quantum efficiency and photoconductive gain are the other essential parameters, especially for QWIPs. They will be described one by one in this section.

1.4.1. Responsivity

Responsivity is the ratio of the output signal, either in current or voltage, to the power of the radiation falling on the detector. It is given as

$$R = \frac{signal\ output}{E.A} \qquad (1.11)$$

where R is the responsivity, E is the incidence, and A is the detector area [25]. The product of the incidence and the area gives the total received radiation power of the detector. If the radiation is produced from the modulated power of a blackbody, the ratio is named blackbody responsivity and depends on the blackbody's temperature.

The responsivity measurement does not provide any information regarding the detector's noise. Thus, high responsivity does not always indicate good detector performance. A detector with high responsivity can also have high noise and, therefore, a low signal-to-noise ratio, which makes the detector not preferable for imaging applications.

1.4.2. Noise Sources

An IR detector can have many types of noise sources. Johnson noise, capacitor noise, shot noise, 1/f noise, and G-R noise are some of them.

Johnson noise happens because of the thermal fluctuations in the detector if the operating temperature is above 0 K. It is proportional to the square root of temperature. Since photon detectors' operation temperature is generally low, Johnson noise is negligible for them. However, it is one of the primary noise sources of thermal detectors.

Shot noise stems from the random arrival of photons to the detector. A bias voltage is required to have a shot noise-related current. The following equation gives shot noise spectral density:

$$i_n = \sqrt{2.q.I.\Delta f} \qquad (1.12)$$

where Δf is the frequency bandwidth of the measurement, q is the electron charge, and I is the device current [25]. As expected, shot noise is one of the dominant noise sources of photon detectors [26].

1/f noise, as the name suggests, is inversely proportional to the frequency. Sources of this noise are still under discussion. Since the spectral density of 1/f noise is higher at low frequencies, if present, it prevents detectors from operating at low frequencies.

G-R noise is the result of the fluctuations in the free carrier density. Carrier concentration variations happen due to the random nature of generation and recombination [26]. The former can occur because of both thermal and optical photon excitations. Expression for G-R noise in a photoconductor is

$$i_{n_{gr}} = \sqrt{4.q.I.g.\Delta f} \qquad (1.13)$$

where g is the gain of the detector [26]. Equation 1.13 is different from the expression of shot noise in terms of the multiplication number, which is 4 in the G-R noise case and 2 in the shot noise case. G-R noise is the dominant noise source for most QWIPs [27].

If the operation temperature of a detector is low enough, generation due to the thermal excitations will be low, and photon-related excitation will be dominant. Thus, Equation 1.13 can be rewritten as

$$i_{n_{photo}} = \sqrt{4.q.I_{photo}.g.\Delta f} \cong \ i_{n_{gr}} \qquad (1.14)$$

where I_{photo} is the current generated by the optical excitations (photons) [27]. This situation is also known as the background-limited performance (BLIP) condition [27].

1.4.3. Noise Equivalent Power

A performance criterion that considers the detector's noise is needed to compare different types of detectors comprehensively. Noise Equivalent Power (NEP) is the radiation flux required to have a signal-to-noise ratio of 1. It can also be expressed as the ratio of noise current or voltage to the current or voltage responsivity, respectively [17]:

$$NEP = \frac{v_{noise}}{R_v} = \frac{i_{noise}}{R_i} \qquad (1.15).$$

Good detectors with low noise and high responsivity have small NEP.

1.4.4. Detectivity

The inverse of the NEP is detectivity. Like NEP, detectivity (D) depends on the detector area and the frequency bandwidth of the measurement. An area and frequency-independent parameter is obtained by multiplying D by the square root of the detector area (A_D) and bandwidth. It is also called specific detectivity (D^*) and can be expressed as [26]

$$D^* = \frac{\sqrt{A_D.\Delta f}}{NEP} = \frac{\sqrt{A_D.\Delta f}}{i_n} R_i \qquad (1.16).$$

Specific detectivity also depends on the received photon flux. Thus, the f/# of the detector system must be shared while giving the specific detectivity values. Like responsivity, D^* measurement is done using a blackbody, and it is called blackbody detectivity.

1.4.5. Noise Equivalent Temperature Difference

Noise Equivalent Temperature Difference (NETD) is the temperature difference between the target and the background needed to get a signal equal to the rms noise voltage. The equation for NETD is

$$NETD = \frac{Noise\ Voltage}{Signal\ Voltage} \Delta T \qquad (1.17)$$

where ΔT is the temperature difference between the test object and its background [26]. NETD measurements are generally done for focal plane arrays and given together with the f/# and integration time information because of the strong dependence.

1.5. Development Phases of Infrared Photon Detectors

With the advancements in semiconductor technologies and the efforts of scientists, IR detector technology took a long path from the first single pixels to very large format multi-band focal plane arrays. Along the way, IR detector technology made transitions between different phases. Each new stage improved the performance of the previous detectors.

1st generation systems included only 1-D scanning-type detectors [2]. The dominant technology of this generation was HgCdTe photoconductive arrays [2].

2nd generation systems were wavelength-sensitive 2-D staring type arrays [2]. Many different format IR detectors were produced during this period, such as mid, large, and very large [2]. HgCdTe, InSb, and QWIPs were the most frequently used technologies [2].

After the 2010s, IR detector system requirements gradually changed, and 3rd generation systems were introduced [2]. They had dual/multi-band detection capability and high operation temperatures (HOT) [2]. HgCdTe, QWIPs, and T2SLs were the standard technologies of this stage [2].

Today, new generation detector studies, called 4th generation, focus on smaller pixel pitches to increase resolution, decrease the cost, and further increase operation temperature [2]. HgCdTe, T2SLs, and barrier structures like nBn are the hot topic technologies of the era [2].

1.6. Scope and Objective

Despite the excellent uniformity, operability, reproducibility, and low cost, standard QWIP loses its superiority over other technologies because of low QE and photoconductive gain. Achieving moderately high QE and gain using a new material system would make QWIP technology a competitive alternative to the other technologies. Material systems such as InP/InGaAs and InGaAs/GaInP/InP with high In mole fraction InGaAs quantum wells were studied excessively by our laboratory in METU [4,34]. Promising results with CE and QE values as high as 70 and 23%, respectively, were reported in these studies. The motivation of this thesis is to produce an MBE-grown MWIR QWIP with the InP/InAs material system on InP substrate, predicting to obtain high QE and gain. It is also planned to make use of the easy growth and high uniformity advantages of the binary material system.

Thanks to the simulations done by Cellek *et al*. [28,35] showing high photoconductive gain of QWIPs with InP barriers and the experimental data in the literature on the band structure of InP/InAs quantum wells [60-63], the InP/InAs

material system is thought to be a new QWIP material with high QE and gain. Practical implementations of these QWIPs in single detector and FPA levels were done as a part of this thesis.

The next chapter gives detailed information about QWIPs in general and a literature survey to compare the current state of the QWIPs with other technologies.

CHAPTER 2

QUANTUM WELL INFRARED PHOTODETECTORS

In this chapter, first, the operation principle of QWIPs will be discussed briefly. Possible material systems and structures for QWIPs will be summarized next. Finally, a comparison of the QWIP technology with other popular IR detector technologies will be presented.

2.1 Operation Principle of QWIPs

A carrier can reside only at discrete energy states in the well when confined between two potential barriers, as shown in Figure 2.1 [29]. Wave functions of these states are found by solving the well-known Schrödinger's Equation

$$-\frac{\hbar^2}{2m^*}\nabla^2\psi(r) + V.\psi(r) = E.\psi(r) \qquad (2.1)$$

where ħ is reduced Planck's constant, m^* is the effective mass of the electron, V is the potential, and E is the energy of the electron [27].

The energy levels can be found using the boundary conditions and finite well approximation [27]. A general solution for the allowed energy levels for confinement in the z-direction is

$$E_n = \frac{\hbar^2 k_z^2}{2m^*} + \frac{\hbar^2}{2m^*}\left(k_x^2 + k_y^2\right) \qquad (2.2)$$

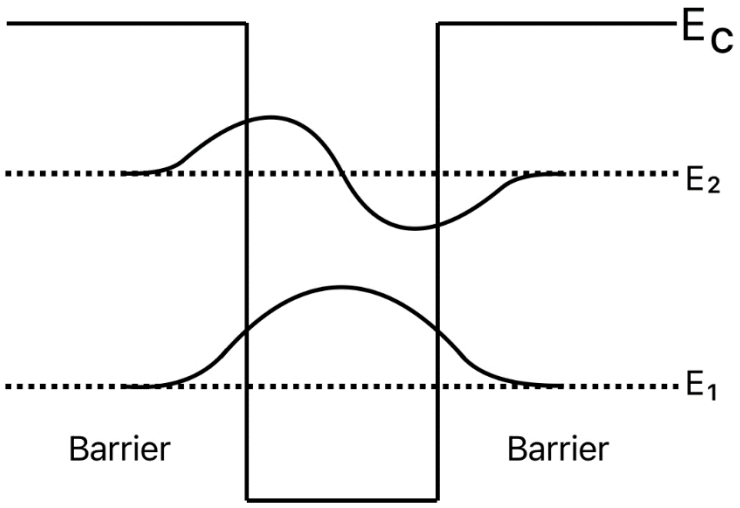

Figure 2.1: Wave functions of the confined states in a QWIP (redrawn after [29]).

where $k_z = \frac{n\pi}{L_w}$ is the wavevector in the z-direction (n is a positive integer), k_x is the wavevector in the x-direction, and k_y is the wavevector in the y-direction [27]. As seen from Equation 2.2, energy levels of the bound states can be adjusted by changing either the well width, L_w, or the semiconductor material system (which changes the effective mass, m^*, in return).

Energy levels are not enough for QE or absorption coefficient calculations. Total transition rate between the states is also needed. It can be found using Fermi's Golden Rule. Assuming there is two discrete energy state in the quantum well, it describes the total transition rate (W) from the first bound state (E_1) to the second (E_2) as

$$W = \frac{\Phi . A . q^2 . h . \sin^2\theta}{4 . \varepsilon_0 . n_r . m^* c} n_{2D} . f . \delta(E_2 - E_1 - \hbar w) \qquad (2.3)$$

where f is the oscillator strength, h is Planck's constant, θ is the angle between the surface normal and the optical beam, and δ is the function governing energy conservation [27]. For $\theta = 0$, the transition rate is zero, meaning normal-incidence radiation cannot cause a transition between the states. Thus, QE, the ratio of the

total transition rate to the total incoming radiation flux, is zero for normal-incidence radiation.

Once the total transition rate is known, the quantum efficiency (η) of the QWIP can be calculated theoretically using the equation [27]

$$\eta = \frac{W}{\Phi . A . cos\theta} = \frac{q^2 h \sin^2\theta}{4\varepsilon_0 n_r c m^* cos\theta} n_{2D} f g(E_2) \qquad (2.4).$$

Most of the QWIPs have one or two bound states for each well. Depending on the level of the second state, three different types of QWIP can be designed. The band diagram of each type is given in Figure 2.2 [30].

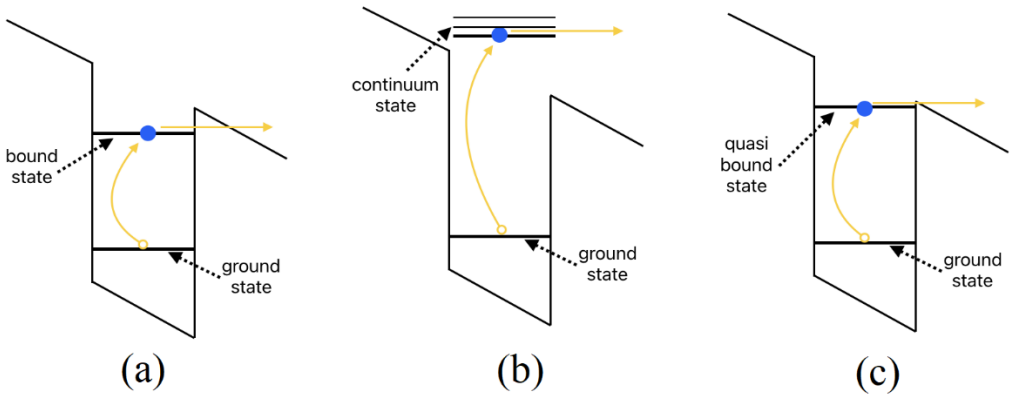

Figure 2.2: Band diagram of three different types of QWIP: (a) bound-to-bound, (b) bound-to-continuum, (c) bound-to-quasibound (redrawn after [30]).

Figure 2.2.a is for the bound-to-bound QWIPs (BB-QWIPs). They have two bound states in the well. They have the narrowest responsivity among the three different QWIP types because of the discreteness of both ground and the first excitation state [27]. Since the excitation state is still below the potential barrier, tunneling is required for the excited electron to contribute to the photocurrent of the detector.

The band diagram of the bound-to-continuum QWIPs (BC-QWIPs) is shown in Figure 2.2.b. They have only one bound state in the quantum well. The excitation

state is above the conduction band level of the barrier material and extended [31]. Thus, they have the broadest responsivity spectrum among the three QWIP types.

The last type is bound-to-quasibound QWIP (BQ-QWIP), shown in Figure 2.2.c. The excitation state level for this type is very close to the conduction band edge of the barrier material. Due to the lower barrier, tunneling is easier for this type than BB-QWIPs. Therefore, the bandwidth of the responsivity spectrum of BQ-QWIPs is between the other two QWIP types [27]. This type is also the optimum regarding the dark-current and bias requirements [27].

Tunneling time can be reduced (due to band-bending) by applying a bias voltage across the detector in BB-QWIPs, as shown in Figure 2.3 [64]. Thus, the responsivity of BB-QWIPs will change nonlinearly with the applied bias [64]. For BQ-QWIPs, a small amount of bias voltage is enough to tunnel the electron through the barrier, and responsivity is slightly nonlinear [64]. For BC-QWIPs, on the other hand, since there is no potential barrier for the excited carrier, the bias voltage is required only to collect them [64]. Therefore, their responsivity spectrum is more linear than other QWIP types [64].

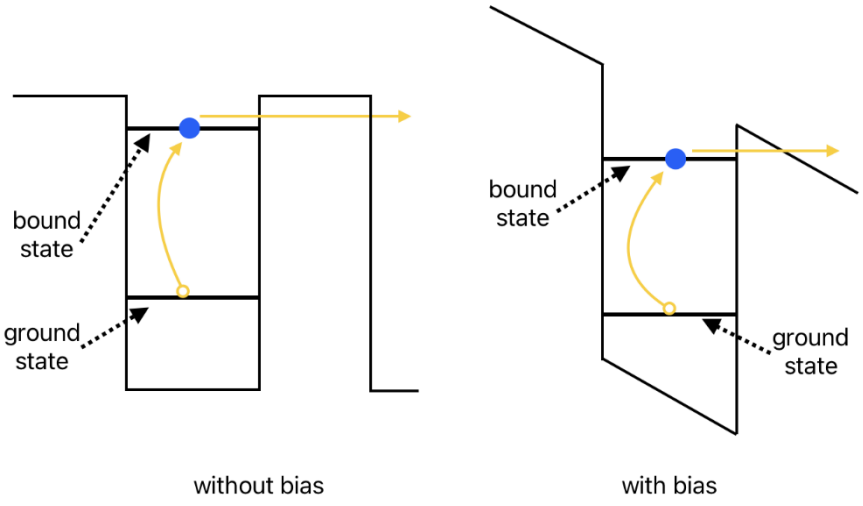

Figure 2.3: Path of the excited electron in the barrier with and without a bias voltage (redrawn after [64]).

For QWIPs, there are mainly three dark-current sources: thermionic emission, thermally assisted tunneling, and ground-state tunneling [32]. They are shown in Figure 2.4 [32]. The first one is the result of thermally excited carriers above the potential barrier and it exponentially increases with temperature. The second one, as the name implies, can happen through tunneling of the thermally excited carriers in the well. Traps in the barrier can facilitate this tunneling. The last one is the result of the tunneling of the carriers in the ground state to the next well and is generally negligible if the barriers are thick enough.

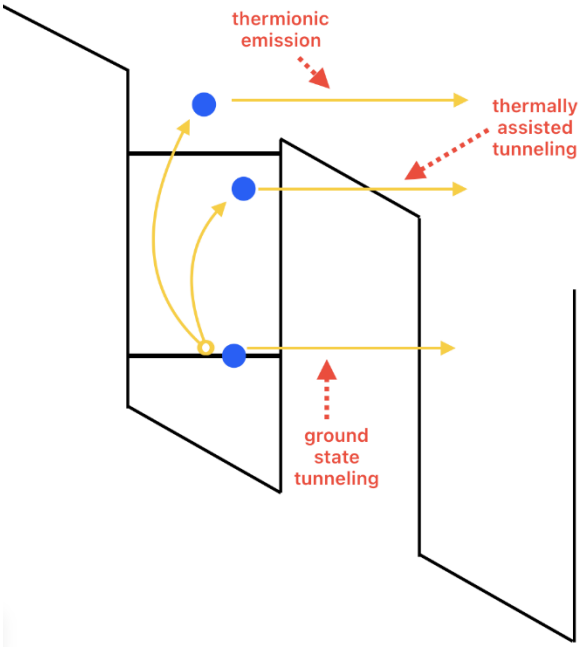

Figure 2.4: Three dark-current sources of QWIPs (redrawn after [32]).

Assuming ground-state tunneling is much smaller than the others, the dark-current of the QWIP is written as [27]

$$I_{dark} = q n_{thermal}(V) v_d(V)\, A \qquad (2.5)$$

where $n_{thermal}$ is the thermally excited electron density, v_d is the drift velocity of the electron, and A is the detector's active area. The critical term in Equation 2.5 is

the $n_{thermal}$. It is strongly temperature dependent. With reasonable approximations, it can be written as

$$n_{thermal} \cong \frac{m^* kT}{\pi \hbar^2 L_p} e^{-\frac{E_b - E_1 - E_F}{kT}} \quad (2.6)$$

where E_b is the conduction band discontinuity, E_1 is the ground-state energy level, E_F is the fermi level, and L_p is the total thickness of one quantum well and barrier pair [27]. Putting together Equations 2.5 and 2.6 results in the following relation [64]

$$\frac{I_{dark}}{T} \propto e^{-\frac{E_b - E_1 - E_F}{kT}} \quad (2.7).$$

This relation is used while determining the activation energy, which is $(E_b - E_1)$, by plotting I_{dark}/T for different temperatures.

For QWIPs, current responsivity is calculated using the equation

$$R_i = q \frac{\lambda}{hc} \eta g \quad (2.8)$$

where g is the detector's gain and η is the quantum efficiency [27]. Gain is the ratio of the photoexcited carriers' lifetime (τ_L) to the time carriers need to travel through the detector (τ_t). Thus, the gain is directly proportional to the drift distance and inversely proportional to the product of L_p and the total number of periods, N. In order to increase gain, N can be decreased or drift distance can be increased. The latter is generally accomplished with increasing bias voltage in QWIPs. Reducing L_p is not preferable since it will increase the dark-current.

The other important term in the QWIP responsivity equation is quantum efficiency, η. It is the product of absorption quantum efficiency, η_a, and escape probability, p_e. η_a is the η described in Equation 2.4. Escape probability is the probability of

excited carriers' escape from the vicinity of the well. It is added to the responsivity equation since excited carriers can make a transition to ground state before contributing to the photocurrent [27]. Increasing N results in higher quantum efficiency. Thus, there is a trade-off between quantum efficiency and gain.

The G-R noise is the dominant noise source in QWIPs and is expressed as [27]

$$i_{G-R} = \sqrt{4q\left(I_{dark} + I_{photo}\right)g\Delta f} \quad (2.9).$$

Depending on the operation condition, either dark- or photo-current can dominate. When the illumination level is low and the operation temperature of the detector is high, the dark-current may be larger than the photocurrent. The opposite is true if the illumination level is high and the operation temperature is low. This second situation is known as the BLIP condition.

Under dark-current limited conditions, specific detectivity is written as [27]

$$D^* = \frac{\eta}{2hc/\lambda}\sqrt{\frac{\tau_L}{n_{thermal}NL_p}} \quad (2.10).$$

Whereas, under BLIP conditions, it is written as [27]

$$D^* = \frac{\lambda_p}{2hc}\sqrt{\frac{\eta_a}{\phi_b}} \quad (2.11).$$

In Equation 2.11, ϕ_b is the number of photons per unit area per second falling on the detector. Since specific detectivity depends on the illumination level, the f/# of the system must also be given for proper comparison.

2.2 Material Systems and Structures for QWIPs in Literature

2.2.1. $Al_xGa_{1-x}As/GaAs$

$Al_xGa_{1-x}As/GaAs$ is the standard QWIP material system for the LWIR band. The bandgap of AlGaAs is adjustable with the Al mole fraction. This makes it possible to produce LWIR QWIPs with different peak responsivity wavelengths. The bandgap energy of $Al_xGa_{1-x}As$ with respect to the Al mole fraction (x) at 300 K is given in Figure 2.5 [33]. Another property of this material system is the nearly constant (around 5.65 Å) lattice constant with changing Al mole fraction as shown in Figure 2.6 [33]. It is nearly lattice-matched with GaAs for all x. Thus, the availability of GaAs substrates with large sizes and low prices makes $Al_xGa_{1-x}As/GaAs$ system a significant IR detector material for the LWIR band in terms of cost. However, conduction band discontinuity (ΔE_C) is not sufficient for the MWIR range, and it becomes an indirect semiconductor beyond x=0.45 as shown in Figure 2.5 [33].

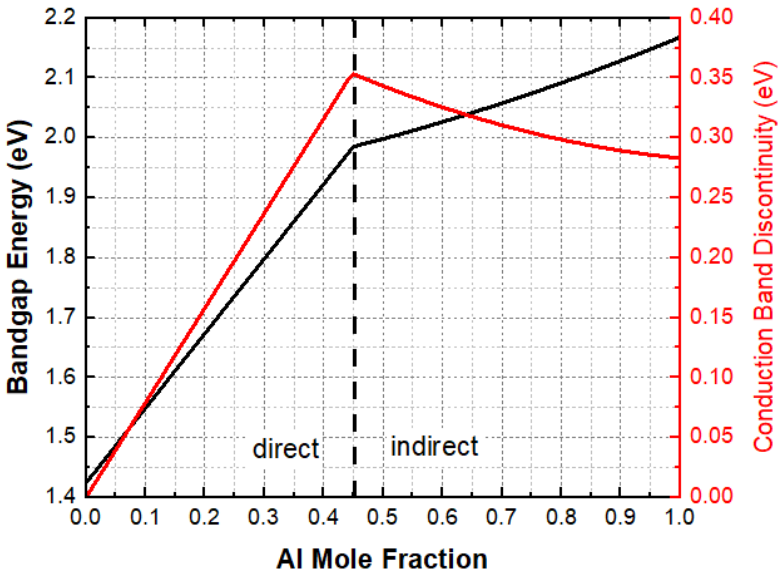

Figure 2.5: Bandgap energy of $Al_xGa_{1-x}As$ and conduction band discontinuity of $Al_xGa_{1-x}As/GaAs$ heterointerface at 300 K (redrawn after [33]).

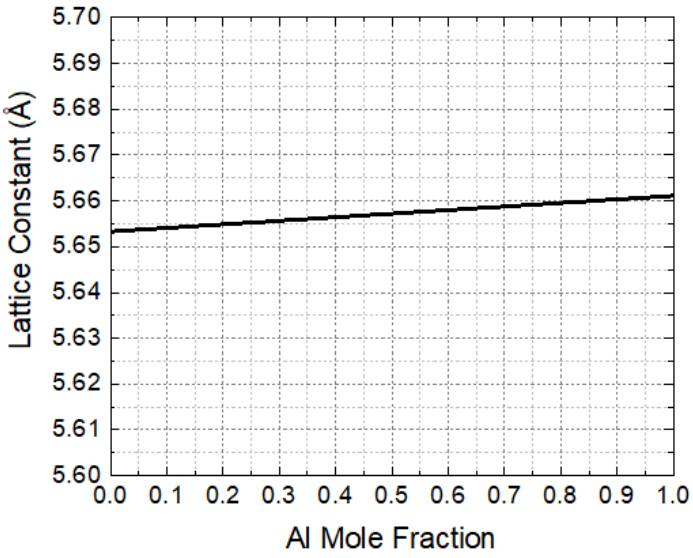

Figure 2.6: Lattice constant of $Al_xGa_{1-x}As$ with changing Al mole fraction (redrawn after [33]).

$Al_xGa_{1-x}As$/GaAs QWIPs' major disadvantages for the LWIR band are their low quantum efficiency due to the quantum mechanical selection rule described in Section 2.1. To overcome this problem, diffraction-gratings are used to manipulate the normal-incidence radiation and force radiation to have an electrical field component normal to the growth direction. Extra layers on top of the top contact, as shown in Figure 2.7 [30], diffract the normal incidence light. Sizes of these patterns are adjusted according to the wavelength of interest in the IR spectrum.

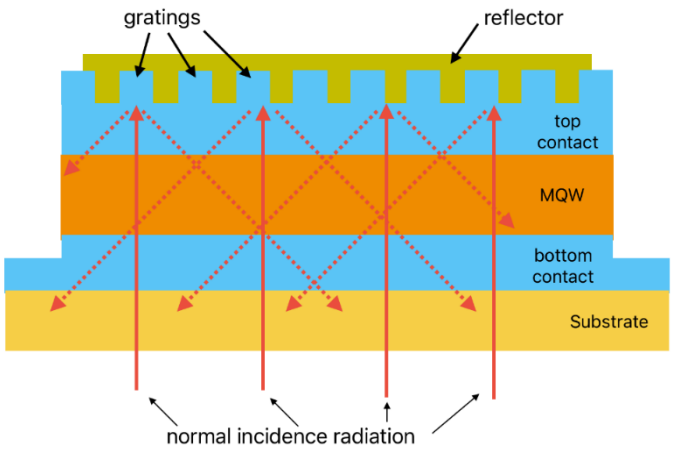

Figure 2.7: Diffraction-gratings and example QWIP structure (redrawn after [30]).

One QWIP example with diffraction-gratings can be given from IRnova company. They produced an LWIR QWIP with a peak wavelength of 10.55 μm using the standard $Al_xGa_{1-x}As/GaAs$ material grown on GaAs substrate with Metal-Organic Vapor Phase Epitaxy (MOVPE) [8]. Produced VGA format FPAs had a pixel pitch of 25 μm. With f/2.7 cold shield and 6.6 ms integration time, they had spatial and temporal NETDs of 13 and 35 mK, respectively. FPA had an operability of 99.87%.

The efficiency of diffraction-gratings drops when the pixel pitch is decreased, which is one of the main requirements of new-generation IR detectors [4]. In addition, they are designed and optimized only for one band [34]. Thus, they are not suitable for dual-band applications.

Another example is corrugated mesa structures developed by Choi *et al.* [5]. They had pyramid-like shapes, as shown in Figure 2.8 [5]. The side walls of the mesas were coated with a metal reflecting layer and a dielectric insulation layer. Refractive indexes of both the metal and the insulator were chosen for total internal reflection. Therefore, incoming normal incidence radiation falling on the side walls is reflected back into the active area of the mesa with a non-zero electric field component along the growth direction. This is also shown in Figure 2.8 [5].

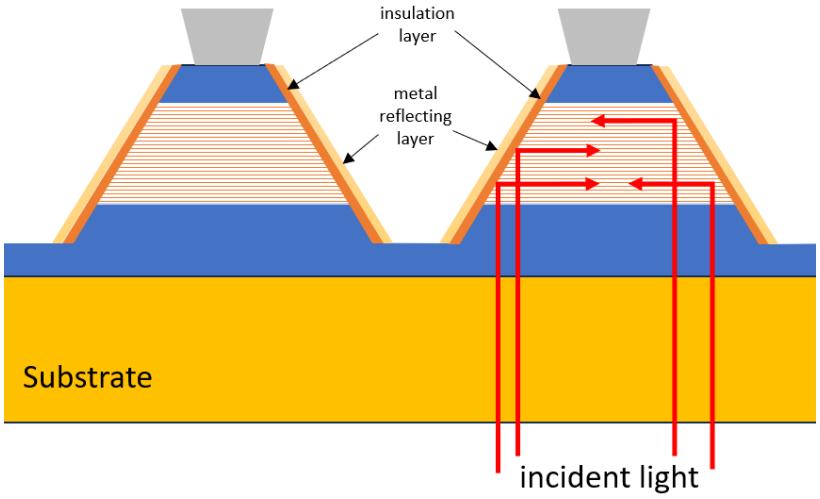

Figure 2.8: Corrugated mesa structures (redrawn after [5]).

One Corrugated QWIP with $Al_xGa_{1-x}As/GaAs/InGaAs$ material system produced by Choi *et al.* [5] showed a peak quantum efficiency of 36.9% with an 8.6 μm cut-off wavelength. It had a NETD value of only 16.1 mK for a 2 ms integration time with f/2 optics. However, the conversion efficiency was only 2.84% due to the low gain of the material system.

Another structure developed by Choi *et al*. [6] to increase QE is the resonator-QWIPs (R-QWIPs). They are a combination of diffraction-gratings and corrugated mesas. The top and side views of the resonator QWIPs are given in Figure 2.9 [6] by illustrating the paths of the incoming radiation. This structure traps the incoming radiation into the mesa, and the radiation starts to resonate inside the mesa until it is absorbed completely. The size and separation of the gratings on top of the mesa are optimized by simulations [6].

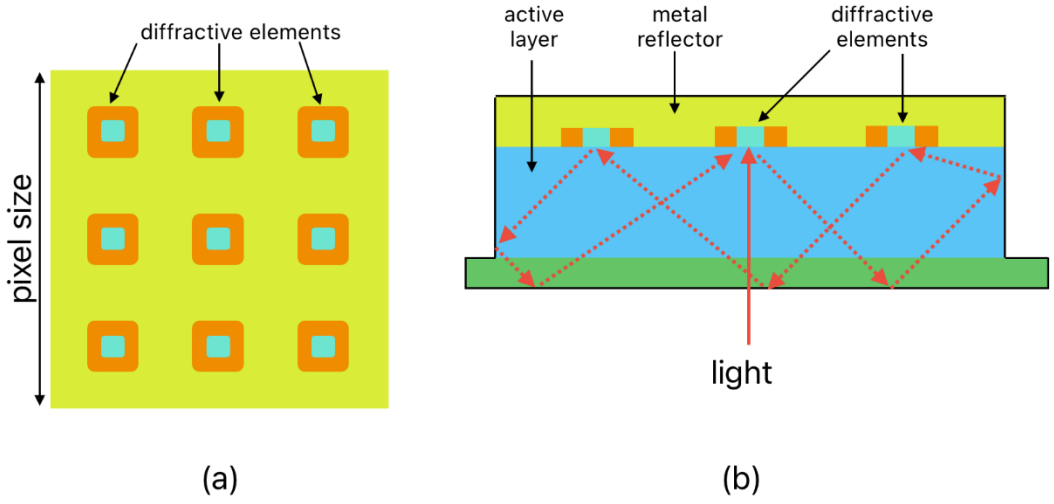

Figure 2.9: The top(a) and side (b) view of the resonator QWIPs developed by Choi *et al*. (redrawn after [6]).

Two different LWIR R-QWIPs were fabricated by Choi *et al*. [6] using the $Al_xGa_{1-x}As/GaAs$ material system. For the first one, x was equal to 0.26. It had a peak responsivity wavelength of 8 μm and gave a 56.4% QE under 4 V bias. Conversion efficiency, on the other hand, was 14% due to the low gain of the material system. FPA produced with this material had a NETD of 21 mK at 60 K

for 3.2 ms integration time with f/1.4 optic. For the second one, x was equal to 0.218. It had a peak responsivity wavelength of 10 μm and gave a 44.0% QE under a 3.5 V bias. Conversion efficiency was 18.3%, again lower than QE. The calculated NETD for this material was 30 mK at 60 K for a 3.8 ms integration time with f/2 optics.

In summary, QWIP with $Al_xGa_{1-x}As/GaAs$ material system needs radiation with non-zero electric field component in the growth direction and has low photoconductive gain. Even though the electric field requirement is fulfilled with unique optical structures, the low gain problem continues, preventing it from being the perfect material for QWIPs.

2.2.2. InP/InGaAs

$InP/In_{0.53}Ga_{0.47}As$ material system lattice matched to InP is another option suitable for LWIR QWIPs with a fixed bandgap discontinuity. Cellek *et al*. [28, 35] showed that the InP/InGaAs material system is superior to the standard AlGaAs/GaAs material system regarding photoconductive gain by doing Monte Carlo simulations. The high gain of the InP/InGaAs material system was attributed to the larger excited electron lifetime in the device. Due to the high gain, the peak CEs of the QWIPs using the $InP/In_{0.53}Ga_{0.47}As$ material system are larger than those of the QWIPs using the standard AlGaAs/GaAs material system.

Cellek *et al.* [35] reported an LWIR QWIP with $InP/In_{0.53}Ga_{0.47}As$ material system. It had a peak responsivity and conversion efficiency of 2.9 A/W and 46%, respectively, at λ_p=7.85 μm for normal incidence radiation under -3 V bias and 77 K operation temperature with diffraction-gratings. The FPA fabricated with the same material, operating at 70 K, had a NETD value of 36 mK with f/1.5 optics and 11 ms integration time.

The cut-off wavelength of the lattice matched $InP/In_{0.53}Ga_{0.47}As$ material system is limited to around 8.5 μm [39]. In order to increase the cut-off wavelength, strained

InP/$In_{0.48}Ga_{0.52}As$ material system can be used instead [39]. Arslan *et al.* [67] reported a LWIR QWIP with diffraction-gratings using this material system. The cut-off wavelength of the detector was around 9 μm. It had a peak responsivity and quantum efficiency of 1.5 A/W and 31%, respectively, for normal incidence radiation under 3.5 V bias. The FPA fabricated with the same material, operating at 67 K, had a NETD value of ~30 mK with f/2 optics and 1 ms integration time.

2.2.3. $Al_xGa_{1-x}As/In_yGa_{1-y}As$

Due to the insufficient conduction band discontinuity and indirect semiconductor behavior beyond x=0.45, the mature $Al_xGa_{1-x}As$/GaAs material system is unsuitable for the MWIR band. Band discontinuity is increased by adding In to the GaAs wells since the bandgap energy of $In_yGa_{1-y}As$ decreases with the increasing In mole fraction. With this approach, bandgap energy differences needed for the MWIR band are achieved. However, this creates a strain problem due to the lattice mismatch between GaAs substrate and $In_yGa_{1-y}As$ wells for any non-zero In mole fraction.

An MWIR QWIP example using $Al_xGa_{1-x}As/In_yGa_{1-y}As$ material system was studied by Tidrow *et al*. [36]. It had 20 periods of $Al_{0.38}Ga_{0.62}As$ barriers and $In_{0.35}Ga_{0.65}As$ quantum wells on GaAs substrate. It had a peak responsivity of around 0.20 A/W at λ_p=4.6 μm for normal incidence radiation under -4 V bias and 77 K operation temperature without a diffraction-grating.

Arslan *et al*. [66] fabricated a voltage-tunable dual-band (MWIR/LWIR) QWIP on a GaAs substrate. Optical grating structures whose sizes optimized for the LWIR band were created on the detector. $Al_{0.36}Ga_{0.64}As/In_{0.21}Ga_{0.79}As$ material system was used for the MWIR stack. Thin GaAs layers were inserted between the quantum well and the barrier. With a bias of 2 V for the MWIR band, the detector had a peak responsivity of 0.150 A/W at λ_p=5.1 μm for normal incidence radiation at 77 K operation temperature.

2.2.4. $Al_{0.48}In_{0.52}As/In_{0.53}Ga_{0.47}As$

The $Al_{0.48}In_{0.52}As/In_{0.53}Ga_{0.47}As$ material system lattice matched to InP is another option for MWIR QWIP. It has a fixed conduction band discontinuity of 0.5 eV under lattice matched compositions. Only the thickness of the well can be changed to adjust the cut-off wavelength.

A QWIP with $Al_{0.48}In_{0.52}As$ barriers and $In_{0.53}Ga_{0.47}As$ quantum wells grown on an InP substrate was reported by Hasnain *et al*. [37]. It had a peak responsivity of around 20 mA/W at λ_p=4 μm for normal incidence radiation under 4 V bias and 10 K operation temperature. The peak QE was about 5.5%, which was still low.

Another QWIP with $Al_{0.48}In_{0.52}As/In_{0.53}Ga_{0.47}As$ material system on InP was reported by Kaldirim *et al*. [65]. Optical grating structures were defined on the detector. It had a peak responsivity of around ~70 mA/W at λ_p=4.25 μm for normal incidence radiation under 3 V bias and 80 K operation temperature. The peak QE and detector gain were 4% and 0.5, respectively, resulting in only 2% conversion efficiency.

2.2.5. High-x $InP/In_xGa_{1-x}As$

Standard GaAs-based material systems mentioned previously have given low conversion efficiencies because of the normal incidence radiation detection inability and low photoconductive gain. On the other hand, high-x $In_xGa_{1-x}As$ quantum wells seem to have shown a higher degree of detection ability for normal incidence radiation [12, 13, 47]. Peng *et al*. [12] studied the lattice-matched $Al_{0.48}In_{0.52}As/In_{0.53}Ga_{0.47}As$ and strained $AlAs/In_{0.7}Ga_{0.3}As$ material systems and observed intersubband transitions in the InGaAs quantum wells caused by S-polarized light (also known as transverse electric field [TE] polarized light or normal incidence radiation). Karunasiri *et al*. [13] also reported TE polarized light absorption in strained n-type GaAs/InGaAs LWIR QWIP and ascribed this

observation to spit-orbit coupling that can cause spin-flip intersubband transitions. Normal incidence radiation detection of QWIP was also attributed to macroscopic light scattering from the device edges and other rough features on the chip and to microscopic light scattering by quantum well interface roughness [54]. Liu *et al*. [54] designed a unique experimental setting to have negligible macroscopic light scattering and used two different QWIPs (an LWIR QWIP with GaAs quantum wells and a MWIR QWIP with $In_{0.1}Ga_{0.9}As$ quantum wells). They determined the ratio of S-polarized light to P-polarized light (mix of TE and transverse magnetic field, TM) in the photoresponse of the QWIPs. The ratios were 0.2% and 3% for GaAs and InGaAs quantum wells, respectively. The difference in the band mixing strength of the well materials was considered as the main reason for the higher absorption in InGaAs quantum well for TE polarized light. Last but not least, Hernando *et al*. [55] studied the normal incidence radiation absorption of $GaAs/In_xGa_{1-x}As$ for different In mole fractions in the range of 0.25 to 0.4 [55]. They observed a rise in the TE/TM responsivity ratio from 5 to 8% for In mole fraction increasing from 0.25 to 0.4.

Studies given above suggest that InGaAs quantum wells have the ability to absorb normal incidence radiation, and this absorption can be increased further by using a higher In mole fraction. Studies also show that the photoconductive gain of the $InP/In_xGa_{1-x}As$ material system on InP is higher than that of the GaAs-based material systems. Monte Carlo simulations done by Cellek *et al*. [28, 35] demonstrated that InP barrier material provides higher device gain. These two properties of the $InP/In_xGa_{1-x}As$ material system make it an important candidate for high conversion efficiency QWIP material.

A high-x $InP/In_xGa_{1-x}As$ (x=0.83) grating-free 15-μm pitch 640x512 MWIR QWIP FPA with GaInP layers between the well and barriers (for spectrum adjustment) was reported by Besikci [34, 47]. The pixels exhibited a peak quantum efficiency of 23% and a peak conversion efficiency of 40% at 80 K with f/2 optics. It also had a specific detectivity of $1x10^{11}$ $cmHz^{1/2}/W$ at the same conditions.

Another grating-free MWIR QWIP with InP/$In_{0.85}Ga_{0.15}As$ material system was reported by Besikci and Balcı [4]. It had a peak quantum efficiency of ~22% and a peak conversion efficiency of ~70% under -3.5 V bias voltage at 78 K with f/2 optics. It also had a specific detectivity of ~$1.5x10^{11}$ $cmHz^{1/2}/W$. The FPA processed from the same material by Besikci *et al*. [16] yielded 24.4 mK mean NETD with f/2 optics and 13 ms integration time for half-filled ROIC capacitors while looking at a 300 K background and operating at 70 K. The FPA pixel pitch was 15 μm. Test pixels with variable areas were also processed and characterized. The dark- and photo-currents of the pixels were shown to be scaled perfectly with the pixel area, demonstrating the absence of an edge-coupling effect. Thus, the high conversion efficiency of the InP/$In_{0.85}Ga_{0.15}As$ material system seems to be the result of normal incidence radiation detection ability and high device gain.

2.2.6. Proposed InP/InAs Material System

To the author's knowledge, no QWIP has been made using the InP/InAs material system so far. However, studies on lasers and nanowires with InP/InAs quantum wells or quantum dots are present in the literature. These studies can be used to determine the band structure of the InP/InAs quantum wells for MWIR QWIP production.

Wang and Stringfellow [60] studied the effect of strain on InP/$Ga_xIn_{1-x}As$ single quantum wells and calculated the conduction-band discontinuity (ΔE_C) of InP/InAs as 0.4 eV. Schneider and Wessels [61] calculated the valence and conduction-band offsets of InP/InAs quantum wells as 270 and 630 meV, respectively. The authors also showed that these values were in accordance with the experimentally obtained photoluminescence peaks. Holm and Pistol [62] estimated the band diagram of InP/InAs quantum dots with a height of 12 nm and found ΔE_C around 0.38 eV.

Mohan *et al*. [63] reported a nanowire structure containing InP/InAs quantum wells. The authors calculated the ΔE_C as 0.33 eV by considering the strain.

An MWIR detector with a responsivity spectrum in the 3-5μm wavelength range and a peak responsivity at 4 μm needs an intersubband transition energy of 0.31 eV. The conduction-band discontinuity values of InP/InAs quantum wells and dots mentioned above are in the range of 0.33-0.63 eV and, thus, suitable for MWIR detector production.

As discussed in Section 2.2.4, for $In_xGa_{1-x}As$ quantum wells, absorption of normal incidence radiation increases with increasing In mole fraction. Thus, a higher absorption is expected at the upper limit of In mole fraction, corresponding to InAs quantum wells. With this motivation, a MWIR QWIP with an InP/InAs material system is proposed for this thesis study.

2.3 MWIR Detectors – State of the art

Many different IR detector technologies and materials have been used in the MWIR band throughout history, such as InSb, HgCdTe, and QWIPs. Several new ones, such as T2SL and *X*Bn barrier detectors, are also under study. This section will give the current status of the MWIR detector technologies and materials.

2.3.1. InSb

Quantum efficiencies of InSb photodiodes increased above 90% over time [38]. FPA pixel operability as high as 99.9% was shown [38]. NETD values less than 20 mK were achieved [38]. However, operation temperatures are still low, around 80 K [38]. Current studies of InSb focus on pitch reduction and lowering dark-current to increase operation temperature [10]. Some of the state of the art InSb detectors are summarized in Table 2.1 [38].

One recent example is the Blackbird integrated detector dewar cooler assembly (IDDCA) [78]. 10 μm pitch 1920x1536 format FPA has an NEDT value of 22.5 mK with f/4 optics and an operability value of higher than 99.5% [78]. The quantum efficiency of the pixels is higher than 80%, with a dark-current of less than 0.8 pA at 77 K [78].

Table 2.1: State of the art InSb detector characteristics.

Manufacturer	Format	Pitch (µm)	Frame Rate (Hz)	Operation Temp. (K)	NETD (mK)	Operability (%)
Sofradir [77]	VGA	15	-	80	20	> 99.7
SCD [78]	1920x1536	15	-	77	22.5	> 99.5
FLIR [79]	VGA	15	60	-	< 25	-

2.3.2. HgCdTe

HgCdTe is the most mature and frequently used MWIR detector technology. High quantum efficiency and adjustable cut-off wavelength make HgCdTe an important IR detector material. Growing high-quality HgCdTe was a challenge in the past. Today, it is relatively easy to grow HgCdTe on CdZnTe substrates. However, CdZnTe substrates are expensive and hard to find due to the limited number of producers [39]. In addition, finding a large area high-quality CdZnTe substrate is difficult [38].

Recent studies of HgCdTe focus on smaller pixel sizes and alternative substrates to lower the cost and make it readily accessible [39]. However, the lattice mismatch between the HgCdTe and alternative substrates makes the operability level relatively low. In addition, for low crosstalk between adjacent pixels, the fully depleted and thin absorber layer requirement limits the QE [4]. The QE of HgCdTe

MWIR detectors ranges around 60-80%, and dark-currents are lower than the "Rule-07" heuristic [40].

Nowadays, 5 μm pitch high frame rate HgCdTe FPAs are available [41]. Some of the state of the art HgCdTe FPAs are summarized in Table 2.2.

Table 2.2: State of the art HgCdTe FPA characteristics.

Manufacturer	Frame Rate (Hz)	Pitch (μm)	f/#	Operation Temp. (K)	NETD (mK)	Operability (%)
DRS [42]	30	6	2.6	-	< 30	>99.5
Selex [43]	120	8	2.8	110	20	>99.8
Sofradir [44]	60	15	5.5	100	20	99.8
AIM [45]	-	15	-	-	25	>99.5

2.3.3. Type-II Superlattice

Type-II Superlattice is currently the hot topic of the IR detector area. Most scientists work on this technology. InAs/GaInSb and InAs/GaSb on GaSb are critical material systems for T2SL structures. They are also used as an absorber layer in the *X*Bn barrier detectors, which have low dark-currents and high operating temperatures [38]. Promising results have already been achieved, especially in the MWIR band [46].

One of the continuing problems for T2SL is obtaining high-quality thick absorber layers with enough diffusion length to decrease optical crosstalk between the spectral windows for dual-band applications [4]. Another one is the low QE and high dark-currents in the LWIR band, which limits the performance of dual-band applications [10].

Quantum efficiencies of T2SL detectors in the MWIR band, varying between 25-80%, approach that of HgCdTe detectors [40]. Dark-currents, however, are still

high, nearly ten times larger than the “Rule-07” heuristic [40, 48]. On the other hand, T2SL InAs/GaSb nBn MWIR detectors have NETD values similar to HgCdTe up to 150 K [48]. Some of the state of the art T2SLdetectors are summarized in Table 2.3.

Table 2.3: State of the art T2SL MWIR FPAs.

Manufacturer	Frame Rate (Hz)	Pitch (μm)	f/#	Operation Temp. (K)	NETD (mK)	Operability (%)
IRCameras [49]	475	20	2.3	-	< 35	> 99.8
IAF [51]	-	40	-	78	< 26	-
JPL [50]	-	24	2	160	18.7	99.7

2.3.4. Quantum Well Infrared Photodetectors

Because of the low conversion efficiencies of the standard QWIP material systems, the attention of most researchers in the infrared photon detector area has been turned to new technologies like T2SL and *X*Bn barrier detectors. Thus, the number of QWIP detectors in the literature, especially in the MWIR band, is lower than that of the other hot topic technologies. And yet, there are still MWIR QWIPs having performances comparable with the T2SL and HgCdTe in FPA level [39].

In the literature, the quantum efficiencies of MWIR QWIP detectors vary between 4 and 28% [4, 40, 54, 55]. Nevertheless, as high as 70% conversion efficiency has been achieved using alternative material systems without diffraction-grating or special mesa structures [4]. Dark-currents, on the other hand, are larger than the state of the art HgCdTe and T2SL detectors [40]. For the FPA-level operation, NETD values lower than 20 mK and operability values greater than 99% have been obtained, as shown in Table 2.4.

Table 2.4: Some examples of MWIR QWIP FPAs.

Manufacturer	Integration Time (ms)	Pitch (μm)	f/#	Operation Temp. (K)	NETD (mK)	Operability (%)	Material System
Sofradir and Thales [56]	20	25	2	90	34	99.7	
QmagiQ [57]	17.78	40	2.3	68	40.1	99.74	InGaAs/ AIGaAs
JPL [58]	60	19.5	2.5	90	23	99.95	InGaAs/ AIGaAs
Schneider *et al* [59]	20	24	1.5	88	14.3	-	InGaAs/ AIGaAs
Beşikci *et al*. [16]	20	15	2	78	< 20	99.3	InP/ InGaAs
Kaldirim *et al*. [65]	20	25	1.5	80	22	99	AlInAs/ InGaAs
Arslan *et al*. [66]	20	25	1.5	65	14	99.5	AlGaAs/ InGaAs

2.4 Comparison of QWIP with Other Technologies

When discrete detector level performance is considered, as seen from the discussions in Sections 2.2 and 2.3, standard QWIPs are inferior to other traditional IR detector technologies in terms of QE and dark-current. However, they give similar or better results regarding the dual/multi-band capability, uniformity, operability, thermal cycling stability, reproducibility, and cost. Among these, uniformity is essential for FPA sensitivity [39]. A system-level performance study shows that an FPA with good uniformity but relatively low QE and high dark-current can have similar range performances compared to an FPA with poor uniformity but high QE and low dark-current [52]. This does not mean that QE and dark-current values are always unimportant at the FPA level. They are still needed for operation conditions with short integration times, high frame rates, or low background radiation [39]. InSb, HgCdTe, and T2SL are superior to the standard QWIP in these conditions.

Another difference between QWIP and the other technologies is the adjustable photoconductive gain of QWIP. It makes adaptation to various operation conditions easier. A discrete sensor's signal-to-noise ratio (SNR) and temporal NETD are gain-independent [53]. However, after the hybridization of an FPA with an ROIC, the integration capacitors' limited capacity makes the overall system's SNR and NETD gain-dependent [47]. When the integration time is adjusted for half-filled integration capacitors, the SNR of QWIP is expressed as

$$SNR = \frac{1}{2}\sqrt{\frac{Q_w}{g}} \qquad (2.12)$$

where Q_w is the number of electrons that the ROIC integration capacitors can hold and g is the detector's gain [53]. In addition, the NETD of QWIP can be calculated using

$$NETD = \frac{T_B}{2}\sqrt{\frac{g}{Q_w}} \qquad (2.13)$$

where T_B is the background temperature [53]. It is clear from Equations 2.12 and 2.13 that lower gain can improve the SNR and NETD when there is enough background photon flux to fill the integration capacitors. On the other hand, when the integration time is limited due to the frame rate, the NETD of QWIP is given by

$$NETD = \frac{n_{Read}}{C_{thermal}\eta g \phi \tau} \qquad (2.14)$$

where n_{Read} is the read-noise, $C_{thermal}$ is the thermal contrast, ϕ is the photon flux, η is the QE, and τ is the integration time [34]. Thus, higher gain values improve the NETD. Overall, the adjustable gain of QWIP, which is not present in other technologies, is an important property to preserve temporal coherence in dual-band sensors [34].

In this chapter, the operation principle of QWIPs is explained briefly. Material systems for QWIPs in literature are discussed together with the proposed InP/InAs material system. The next chapter presents the growth and fabrication of the InP/InAs MWIR QWIP FPA and pixel array.

CHAPTER 3

GROWTH AND FABRICATION OF MWIR QWIP

In this chapter, first, the molecular beam epitaxial growth of the InP/InAs QWIP will be summarized. Then, the fabrication process of the FPA and test pixels will be presented step by step. Production of a fan-out circuit on a Si wafer for the test pixels will also be discussed briefly. In order to measure the electrical and optical characteristics of the FPA pixels, an array of pixels (identical to those of the FPA) was fabricated together with the FPA. The pixel array was hybridized with the fan-out circuit through flip-chip bonding, as shown in Fig. 3.1. Pixel array includes sub-arrays including 5x5 and 7x7 pixels connected in shunt. Wire bonding pads provide electrical connections to the sub-arrays. This configuration allows the characterization of the FPA pixels (with back side illumination).

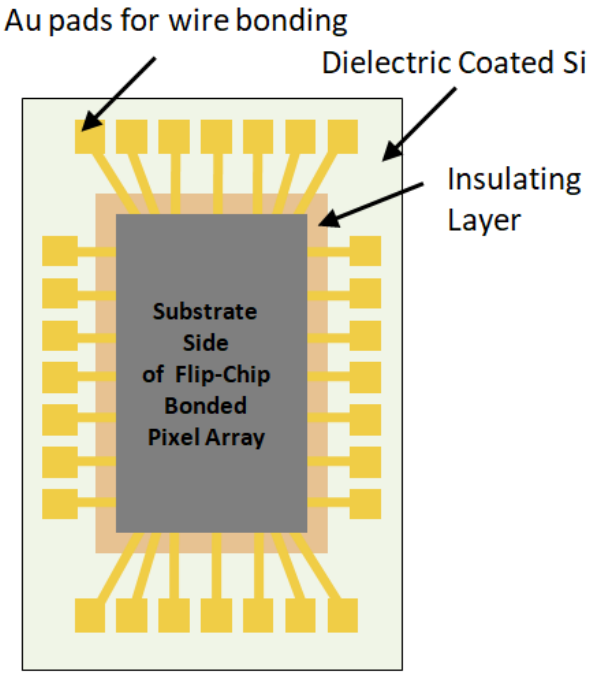

Figure 3.1: Pixel array flip-chip bonded to the fan-out circuit.

3.1 Growth of the InP/InAs QWIP

The epilayer design and growth of the InP/InAs QWIP on the InP substrate was done by Prof. Dr. Cengiz Beşikci using a Riber Epineat III-V MBE system in Quantum Devices and Nanophotonics Research Laboratory of METU. The multi-quantum well (MQW) structure of the InP/InAs QWIP, given in Figure 3.2, consists of ~550 Å InP barriers and ~25 Å Si-doped strained InAs wells.

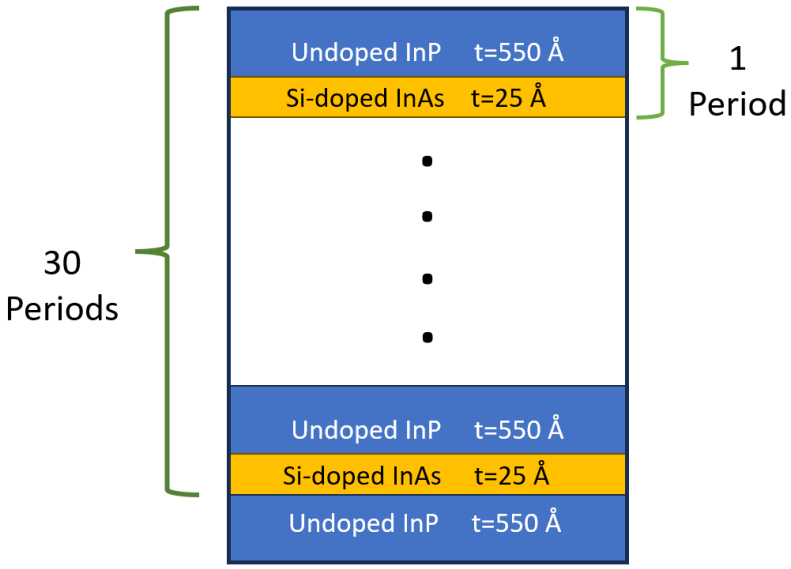

Figure 3.2: Epilayer structure of the InP/InAs QWIP.

3.2 Fabrication Processes

3.2.1 Fabrication of QWIP FPA, Pixel Array and Fan-Out Circuit

The FPA, pixel array, and fan-out circuit were fabricated together with Saadettin Veysel Balcı. The fabrication process used in this work had been developed in the Quantum Devices and Nanophotonics Research Laboratory over the years.

The pixel array and the FPA were produced together using the same wafer. First of all, a lithography mask containing several 640x512 format FPAs and pixel arrays

(with 15 μm pitch) was drawn for different steps of the process. Then, the sample was etched with a wet etchant until the bottom contact to form the individual pixels. The size of the pixels was decreased to 10x10 μm^2 after wet etching. Afterward, metal was deposited on the top of the pixels to form the ohmic contacts and reflectors. Later, the entire sample was covered with a passivation material. The passivation on the previously metal-deposited areas was removed with a proper etchant. Then, under bump metallization (UBM), which facilitates the adhesion of indium and inhibits its diffusion, was applied to the top of the pixels from where the passivation had been removed previously. Lastly, indium bumps, which connect the pixels and the ROIC (or fan-out for pixel array), were generated on top of the pixels using an e-beam evaporator. The pixel array and the FPAs were separated from the wafer using a dicer. The side and top view of the pixel array after each step are shown in Figure 3.3.

A nitride-coated Si wafer was used for the fan-out circuit. The lithography mask used was the same as the pixel array except for the metal paths from shorted 5x5 and 7x7 pixel sub-arrays to the pads where electrical connections were taken by wire bonding. The fabrication process consisted of four steps: metal deposition, passivation, UBM, and indium bump formation. The side and top view of the fan-out after each step is shown in Figure 3.4.

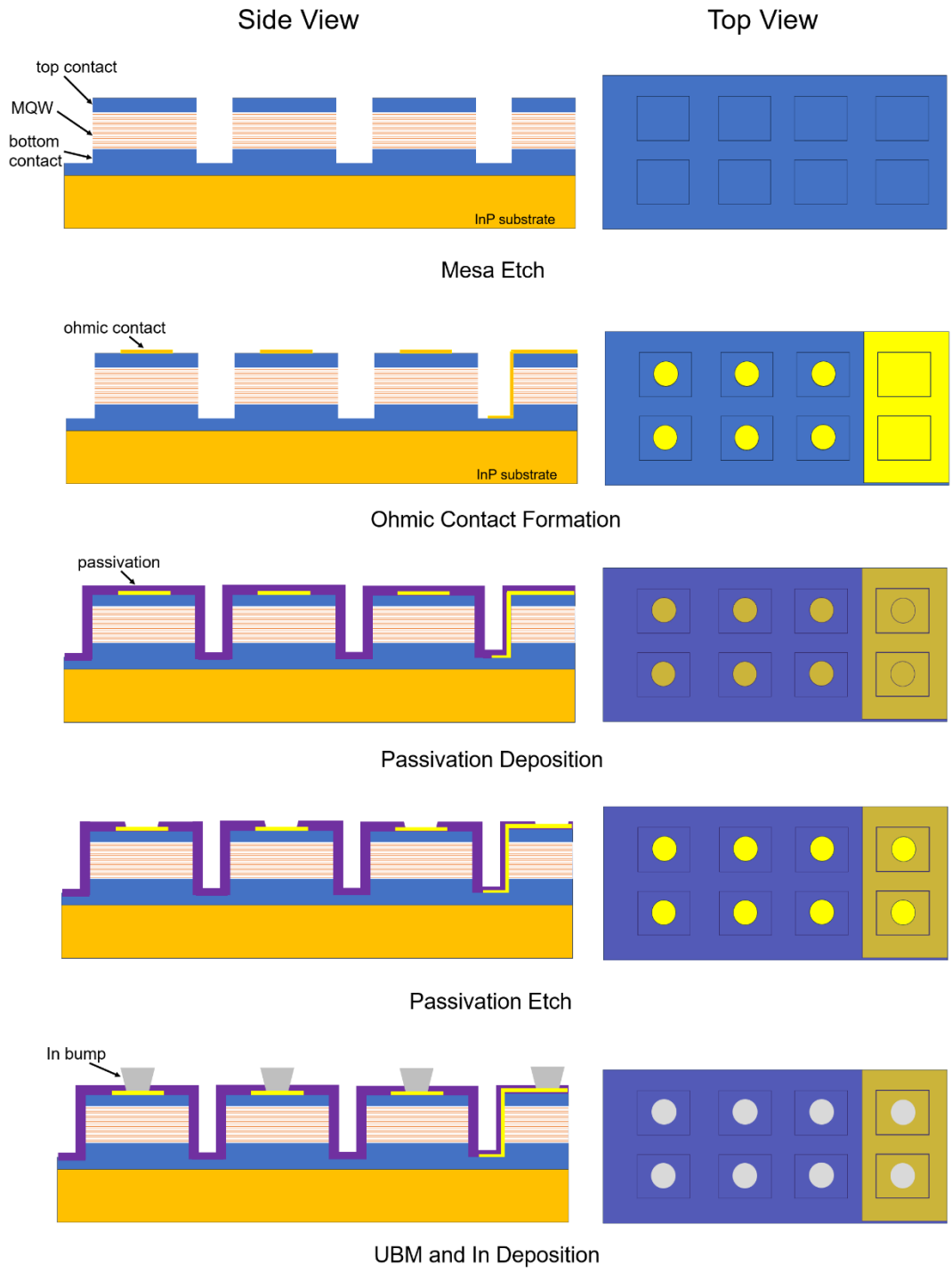

Figure 3.3: Side (left) and top (right) view of the pixel array after each step.

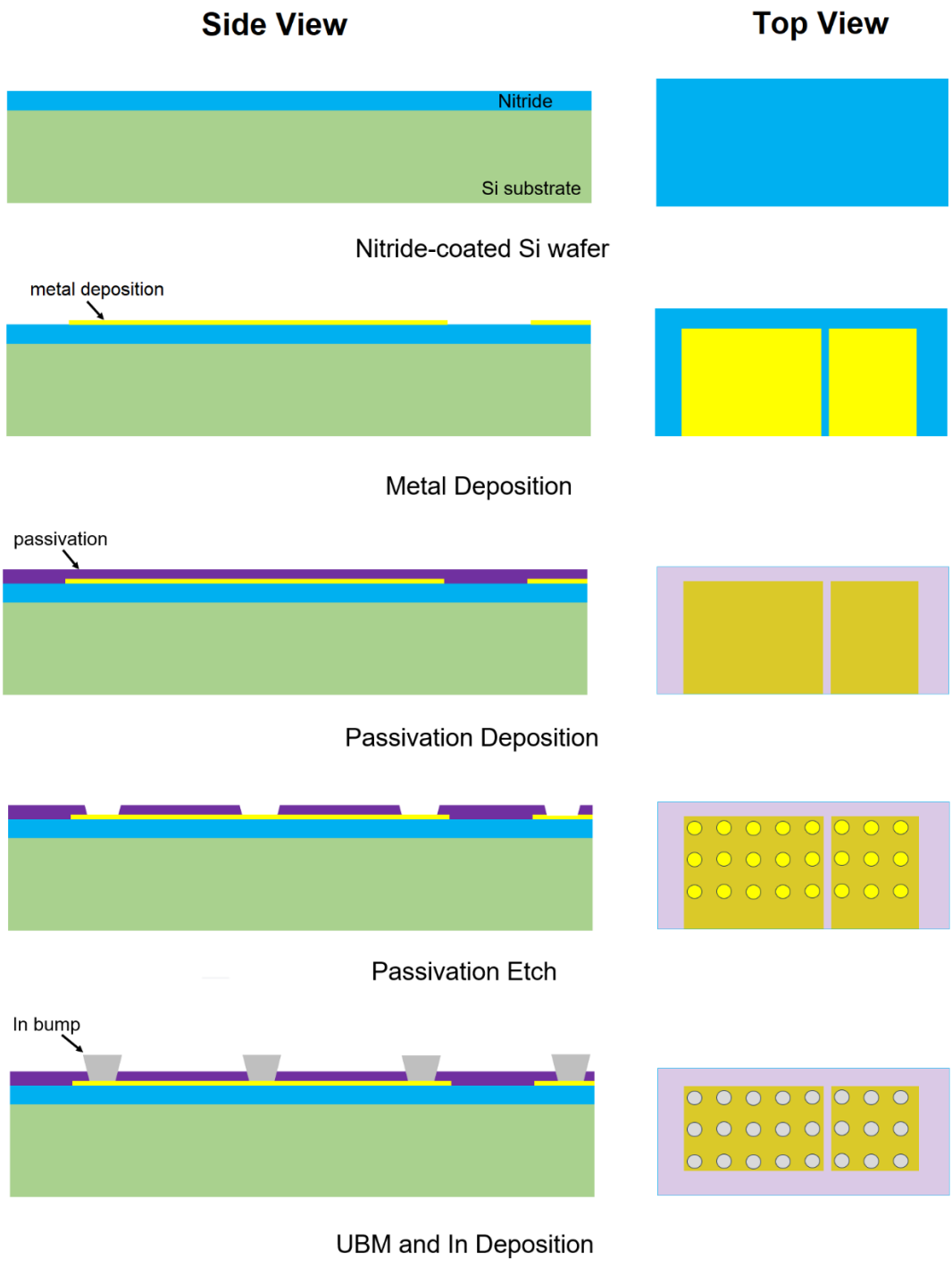

Figure 3.4: Side (left) and top (right) view of the fan-out after each step.

3.2.2 Hybridization and Substrate Thinning

In order to prepare the ROIC for hybrid integration, UBM and In were deposited on the ROIC pixels sequentially. After the fan-out circuit was fabricated and the ROIC was prepared, they were hybridized to the pixel array and the FPA, respectively. Then, underfill material was injected between the FPA and the ROIC and between the fan-out and the pixel array.

The pixel array and the FPA were backside-illuminated, meaning the radiation came from the substrate side. A thick substrate could result in optical crosstalk between the pixels [30]. In addition, since the detectors and ROIC and fan-out were made of different materials and had different thermal expansion coefficients, mechanical stress could lead to cracks or breakages when cooled down to cryogenic temperatures [30]. For these reasons, the substrates of the samples and the FPA were thinned to several tens of microns by mechanical grinding. The side view of the samples after hybridization and substrate thinning is illustrated in Figure 3.5.

After preparing the pixel array and fan-out hybrid, it was placed on a leadless chip carrier (LCC), as shown in Figure 3.6. Electrical connections between the pads of the fan-out and LCC were established with a wire bonder.

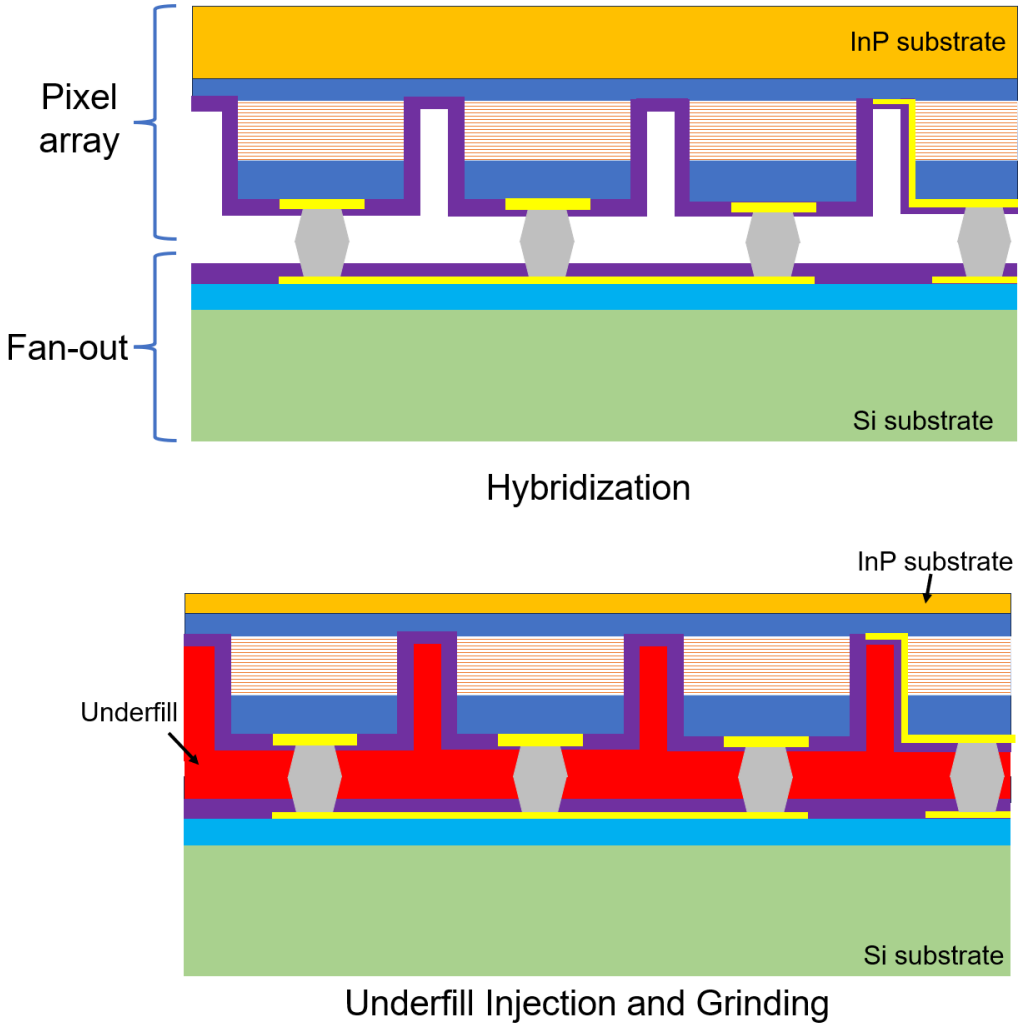

Figure 3.5: The side view of the samples after each process step.

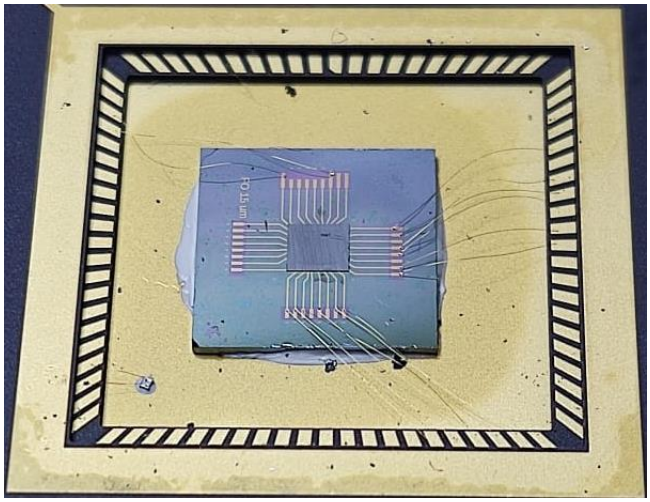

Figure 3.6: Pixel array and fan-out hybrid placed on an LCC.

The FPA and the pixel array were subjected to characterization after the fabrication. The characterization results are presented in the next chapter.

CHAPTER 4

CHARACTERIZATION OF THE MWIR InP/InAs QWIP

This chapter presents the results of the characterization of the pixel array and the InP/InAs MWIR QWIP FPA, which was performed in collaboration with the thesis advisor, Prof. Dr. Cengiz Beşikci. The detailed characterization of the produced FPA was done by Onur Tanış as a part of another thesis study.

Before characterization, the samples were attached to a leadless chip carrier (LCC), and electrical connections to the LCC pads were made using a wire bonder. Characterization was done after placing the LCC into a liquid nitrogen cooled dewar.

4.1 Pixel Array Characterization

Characterization of the pixel array (hybridized to the fan-out circuit) was performed using a source-measure unit, a low-noise preamplifier, a dynamic signal analyzer (for electrical characterization), and an optical test set-up. The optical testing set-up includes a Fourier-transform infrared spectroscopy (FTIR) system, a chopper, a lock-in amplifier, and a blackbody source. Partial loss of the radiation through surface reflection and transmittance of the dewar window were taken into account in the characterization.

Figure 4.1 shows the normalized responsivity spectrum of the pixels under -2 V bias voltage at 80 K. The peak and cut-off wavelengths are ~5.5 μm and ~6.2 μm, respectively. The full width at half maximum (FWHM) of the responsivity spectrum is 1.5 μm and the normalized responsivity spectrum was observed not to be considerably dependent on the bias voltage, both suggesting that the QWIP is a

bound-to continuum type. The low responsivity around 5.8 μm is due to the absorption of the radiation by atmospheric gases.

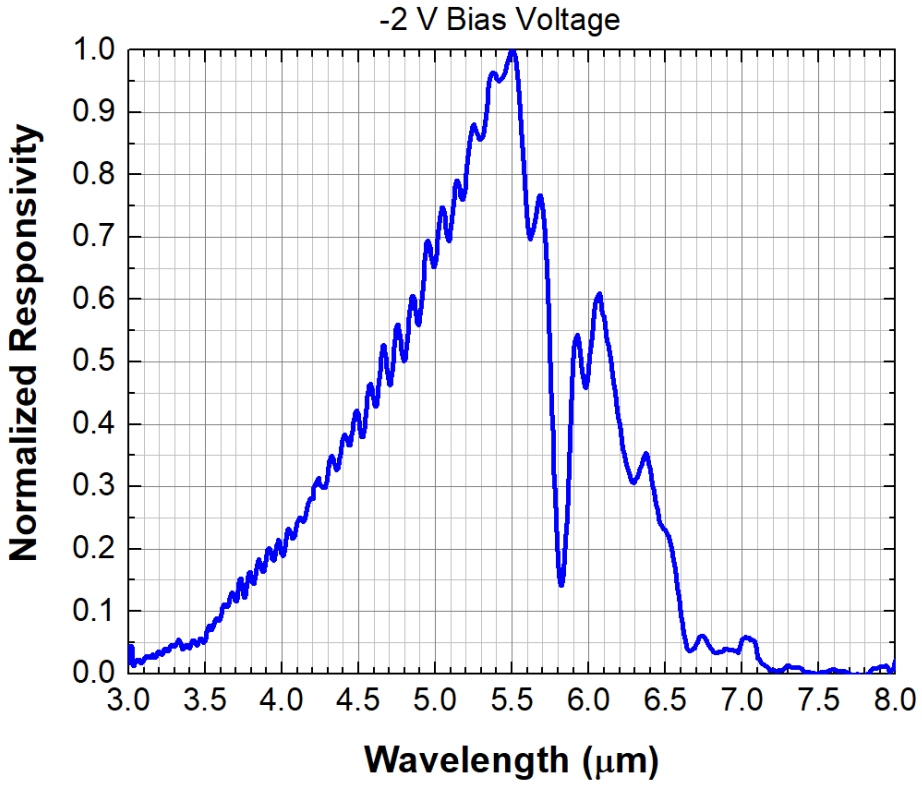

Figure 4.1: Normalized responsivity spectrum of the pixel array.

The results of the dark- and photo-current measurements (recorded with a source-measure unit) are given in Figure 4.2. The characterization was performed on a 5x5 sub-array of pixels. Each pixel had an area of ~100 μm^2. The photocurrent in Figure 4.2 was calculated from the responsivity measurements for f/2 optics and 300 K background temperature. The detectors demonstrated highly BLIP characteristic with f/2 optics at 80 K even under high bias voltages. The BLIP ratio ($I_{photo}/(I_{photo} + I_{dark})$) of the detector was 96% at 80 K under -1 V bias voltage.

Arrhenius plots of the dark current for different bias voltages are given in Figure 4.3. Using Equation 2.7 and the slope of the curves, the dark current activation energy ($E_A = E_b - E_1 - E_F$) of the pixels under 1 V bias voltage was found as 180 meV, which was in reasonable agreement with the optical activation energy

(E_b-$E_1 = 1.24/\lambda_{peak}$) of 225 meV calculated from the responsivity measurements. The Fermi level (E_F) with respect to the ground state energy level can be calculated using Equation 2.6 with the known electron effective mass and quantum well 2D doping density. With an electron effective mass ratio of 0.023 [33] and 2D doping density of 5x10^{11} cm^{-2} for the InAs quantum wells, E_F was calculated as 52 meV above the ground state. This value of E_F was in reasonable agreement with the optical and dark current activation energies.

As expected, the dark current activation energy decreases with increasing bias voltage because of the barrier lowering effect [80]. A lower barrier would result in increased tunneling currents where Equation 2.6 is no longer suitable for dark current calculation [67].

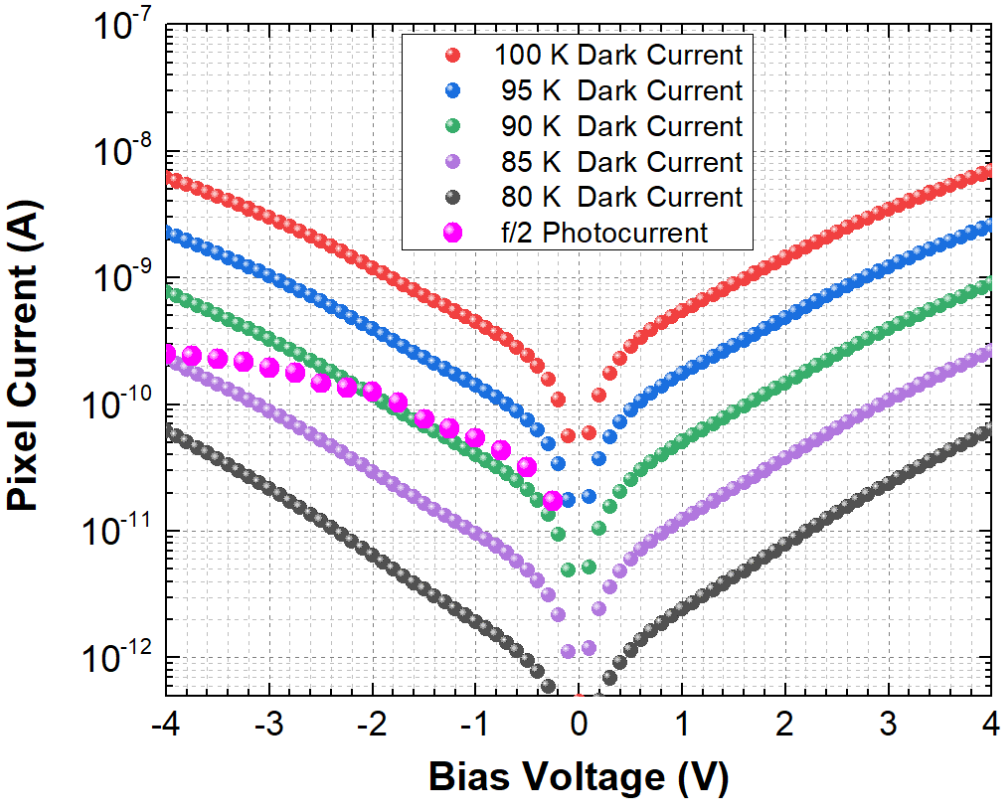

Figure 4.2: Dark- and photo-currents per pixel for different bias voltages.

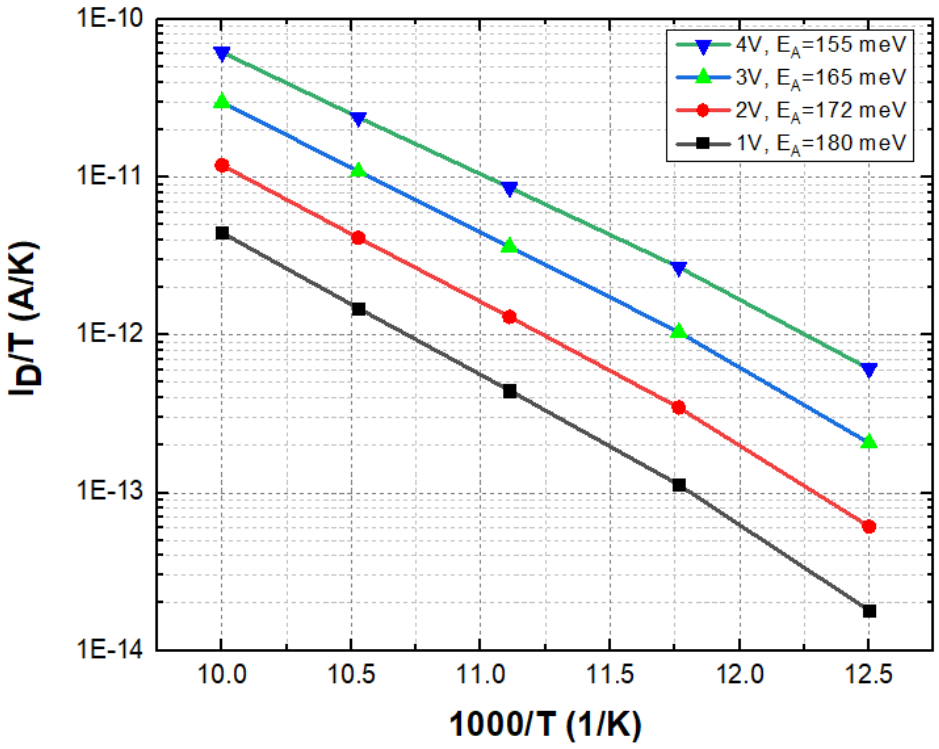

Figure 4.3: Arrhenius plot of the dark current for different bias voltages.

The peak responsivities of the pixels for different reverse bias voltages (mesa top negative) are shown in Figure 4.4, together with the noise gain extracted from the noise measurements using Equation 1.13. Responsivity measurements exhibited a peak responsivity of ~2.7 A/W under -4.0 V bias voltage, corresponding to a peak conversion efficiency of ~61%. This value is higher than the state of the art QWIPs using standard material systems with diffraction-gratings or special mesa structures [5, 6, 37]. The high conversion efficiency, even in the absence of diffraction-gratings, shows the superiority of the InP/InAs material system over standard material systems. The peak conversion efficiency of the pixels for different negative bias voltages is given in Figure 4.5.

As presented in Figure 4.4, the bias dependency of the noise gain is in agreement with that of the responsivity. This observation, together with the other characteristics of the QWIP, suggests that the noise gain is equal to the photoconductive gain. Under this condition, the peak QE of the pixels is extracted

to be ~22% using Equation 2.8. When the broadness of the spectral responsivity is considered, this level of peak QE is exceptional for a grating-free QWIP pixel.

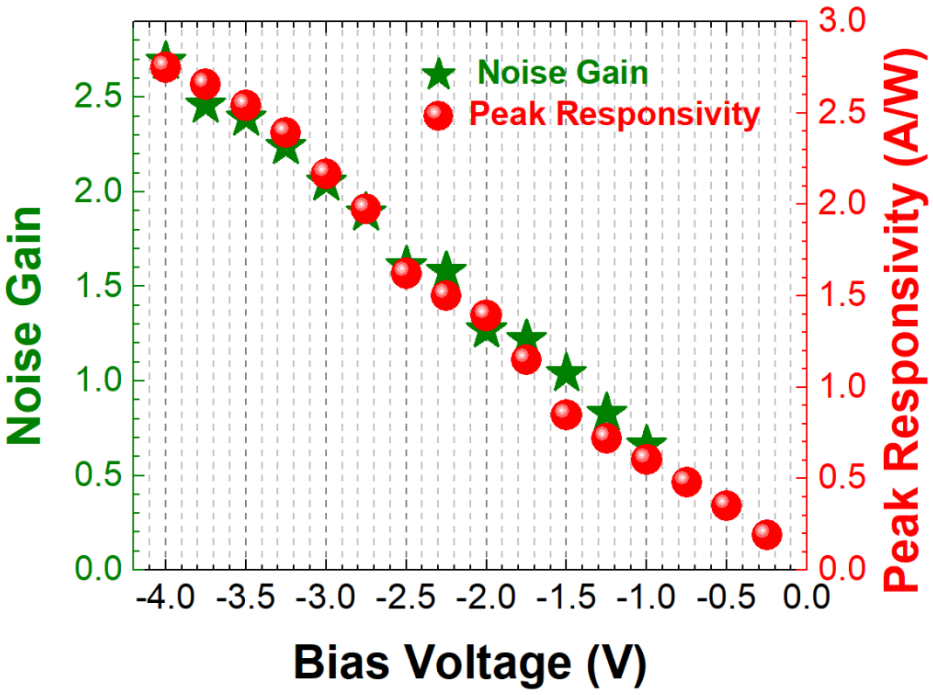

Figure 4.4: The peak responsivity and noise gain of the pixels for different negative bias voltages at 80 K.

The peak specific detectivity was calculated using Equation 1.16, together with the peak responsivity and noise data of the pixels. The peak specific detectivity of the detector for f/2 aperture at 80 K was ~1.5x10^{11} cm$Hz^{1/2}$/Watt under -1 V bias voltage. This level of specific detectivity is sufficient for high performance thermal imaging.

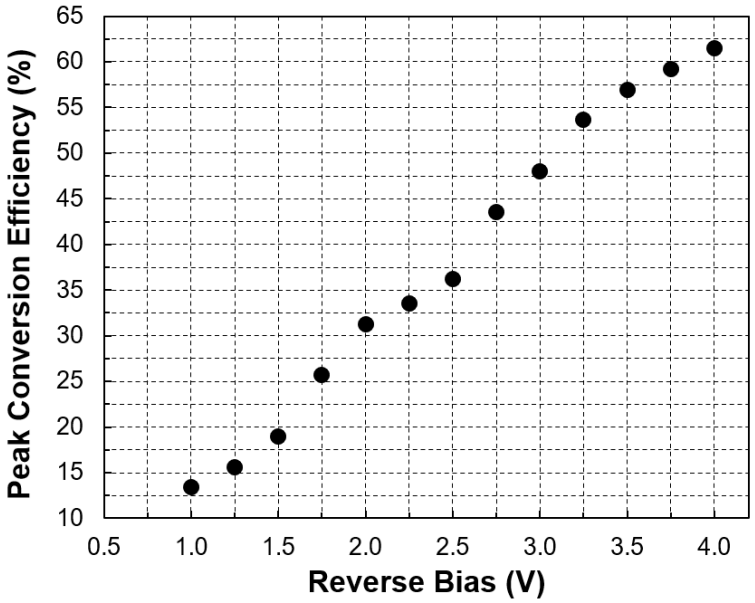

Figure 4.5: The peak conversion efficiency of the pixels for different negative bias voltages.

For comparison with InP/InAs QWIP of this work, the peak QE, responsivity, CE, specific detectivity, and dark current density of QWIPs in the literature using different material systems are listed in Table 4.1. The specific detectivities in the table are for 300 K background temperature and the peak CE values are for the same bias voltage as the peak responsivity. Most of the data in Table 4.1 was taken directly from the related articles. However, some of the responsivity and specific detectivity values were calculated by the author from the reported current and noise gain data. In Table 4.1, θ is the angle between the surface normal and the optical beam.

The QEs of the LWIR QWIPs using AlGaAs/GaAs material system with diffraction-gratings or special mesa structures [5, 6, 68] are similar or higher than that of the grating-free InP/InAs QWIP with similar doping levels. However, the peak responsivities and CEs of AlGaAs/GaAs QWIPs are lower compared to that of the InP/InAs QWIP under the same bias voltage because of the lower photoconductive gain.

The QEs and responsivities of the MWIR QWIPs using AlGaAs/InGaAs material system with or without diffraction-gratings [69, 75] are lower than that of the diffraction-grating-free InP/InAs QWIP even with higher doping level and bias voltage. On the other hand, their dark current densities are lower compared to that of the InP/InAs QWIP under similar or higher bias voltage and detector temperature. The lower dark current density of the AlGaAs/InGaAs material system can be attributed to the higher m^* of the electrons in InGaAs quantum wells (~0.05) compared to m^* in InAs quantum wells (0.023). The relation between the Fermi level (E_F) and m^* is exponential for a given 2D doping density and temperature [27]. Thus, considering Equation 2.6, dark current increases much more rapidly with the temperature or doping density for a smaller m^* [34].

Like AlGaAs/InGaAs MWIR QWIPs, the QEs, CEs, and responsivities of the MWIR QWIPs using AlInAs/InGaAs material system with diffraction-gratings [70-72] are lower than that of the diffraction-grating-free InP/InAs QWIP even with considerably higher doping levels and bias voltages. As a result, the specific detectivities of the AlInAs/InGaAs QWIPs are smaller than that of the InP/InAs QWIP with the same f/#.

InP/InGaP/InGaAs QWIP, reported by Maimon *et al.* [73], had smaller QE, CE, responsivity, and specific detectivity compared to the InP/InAs QWIP even though it was illuminated through a 45° polished facet. It also had a lower dark current density under the same bias voltage and temperature. The reason for these can be the lower quantum well doping density used by the authors.

Table 4.1: Comparison of the QWIPs in the literature with different material systems.

Ref.	Material	Band	Doping (cm^{-2})	pitch (μm)	cutoff (μm)	Quantum Efficiency			Peak Responsivity		CE (%)	Peak Specific Detectivity		Dark Current Density		
						Grating	θ (◦)	η (%)	Bias (V)	R (A/W)		f/#	D* (Jones)	Bias (V)	T (K)	J_d (A/cm^2)
[6]	AlGaAs/GaAs	LWIR	$5.8x10^{11}$	12	8.6	yes	0	56.4	1	0.283	14	2	$9.4x10^{10}$	1	70	$2x10^{-4}$
[68]	AlGaAs/GaAs	LWIR		15	8.9	yes	0	18	1	0.322	4.7			1	77	$8x10^{-4}$
[5]	AlGaAs/GaAs/ InGaAs	LWIR	$4.5x10^{11}$	25	8.6	yes	0	37	11	0.18	2.8	2.2	$1x10^{11}$	11	70	$1.5x10^{-5}$
[67]	InP/InGaAs	LWIR	$2.4x10^{11}$	25	9	yes	0	31	1	0.2	22	2	$4.5x10^{10}$	1	78	$1.7x10^{-4}$
[75]	AlGaAs/GaAs/ InGaAs	MWIR	$4x10^{11}$	19.5	5.1	yes	0	19	1	0.17	4.6	2.5	$4x10^{11}$	1	85	$3.3x10^{-8}$
[69]	AlGaAs/InGaAs	MWIR	$2.1x10^{12}$	24	5.1	no	45	4.8	2.5	0.114	2.7			2.5	77	$3.5x10^{-7}$
[70]	AlInAs/InGaAs	MWIR	$1x10^{12}$	50	4	yes	0	< 10								
[71]	AlInAs/InGaAs	MWIR	$5.2x10^{11}$	25	4.6	yes	0	6.5	4	0.1	2.5	2	$8x10^{10}$	1	80	$1.7x10^{-7}$
[72]	AlInAs/InGaAs	MWIR	$9.2x10^{11}$	25	5.1	yes	0	4	3	0.07	2	2	$7x10^{10}$	1	112	$3.8x10^{-7}$
[73]	InP/InGaP/ InGaAs	MWIR	$1.3x10^{11}$	200	5.1	no	45	4	0.3	0.16	2	0	$3.2x10^{10}$	0.5	90	$3.8x10^{-6}$
[4]	InP/InGaAs	MWIR	$5x10^{11}$	15	6	no	0	22	1	0.9	70	2	$1.5x10^{11}$	1	80	$8x10^{-7}$
This Work	InP/InAs	MWIR	$5x10^{11}$	15	6.2	no	0	22	1	0.6	61	2	$1.5x10^{11}$	1	80	$2x10^{-6}$

The high quantum efficiencies and peak responsivities of the InP/$In_{0.85}Ga_{0.15}As$ [4] and InP/InAs material systems, even in the absence of diffraction-gratings, show the superiority of these material systems for QWIPs over other standard material systems. With higher QEs, peak specific detectivities higher than $1x10^{11}$ Jones are obtained. The CEs of these material systems are also considerably higher than those of the other QWIPs with diffraction-gratings or special mesa structures, making them suitable for operation conditions with short integration times, high frame rates, or low background radiation.

4.2 FPA Characterization

The NETD characterization of the FPA was made using 14-bit imager electronics and a blackbody source at approximately 82 K. The mean NETD of the FPA was measured as ~28 mK with f/1.67 optics at 10 ms integration time. This NETD value is in reasonable agreement with the calculated NETD of ~24 mK based on the electrical and optical measurements on the pixel array. The bias voltage was around -0.55 V and adjusted for half-filled ROIC capacitors during the NETD measurement. This value is very close to the mean NETD value obtained by Besikci *et al*. [16] using an InP/$In_{0.85}Ga_{0.15}As$ MWIR QWIP with the same integration time and optics.

The NETD nonuniformities of the InP/InGaAs [67] and AlInAs/InGaAs [74] QWIP FPAs were higher than 15%. The NETD nonuniformity of the InP/$In_{0.85}Ga_{0.15}As$ [16] QWIP FPA was ~11%. On the other hand, the NETD nonuniformity of the InP/InAs QWIP FPA was only 9.9%, showing the advantages of binary material systems over ternary alloys. The bad pixels, being mostly due to fabrication processes, were not related with the detector material. Figure 4.7 shows an image recorded with the produced FPA with 13 ms integration time and f/2.3 optics after two-point nonuniformity correction (NUC). No bad-pixel replacement was applied to the image.

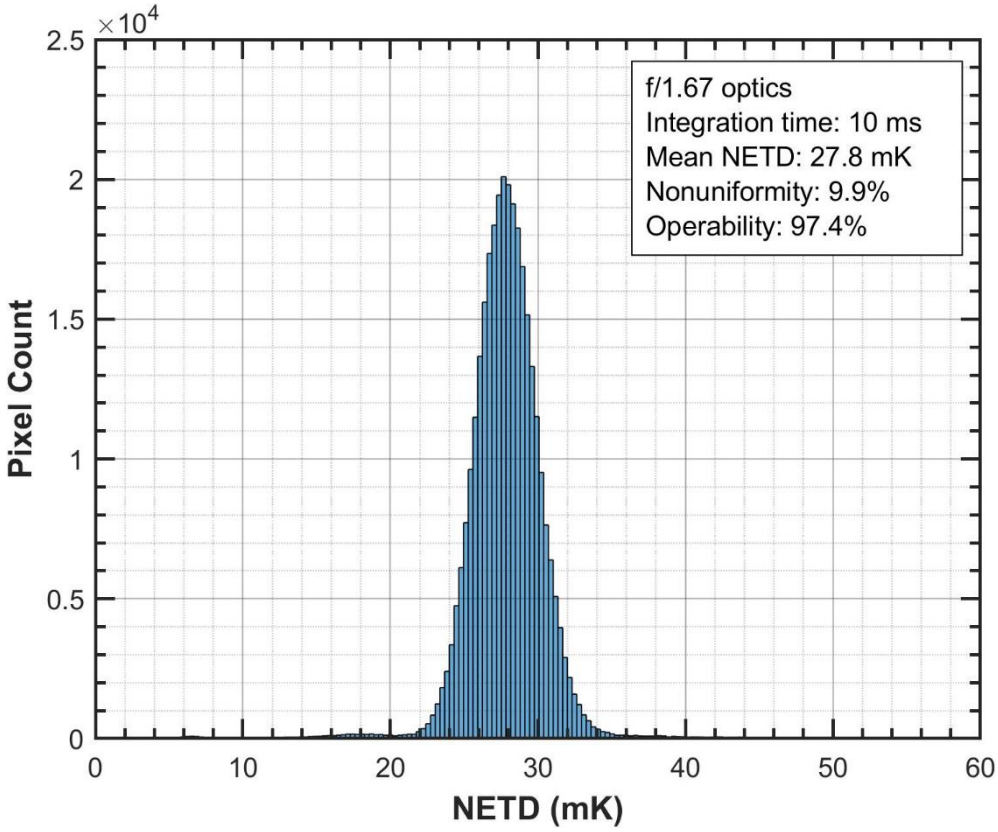

Figure 4.6: NETD histogram of the FPA at 81 K detector temperature.

Figure 4.7: An image recorded with the produced FPA.

In summary, characterization results of the diffraction-grating-free InP/InAs MWIR QWIP both in pixel and FPA level were presented in this chapter. The results were compared with the other QWIPs in the literature. The comparison indicated the advantages of binary InP/InAs material system, such as high CE, QE, detectivity, and uniformity. The next chapter summarizes this thesis work and discusses the possible future work.

CHAPTER 5

CONCLUSION AND FUTURE WORK

In this thesis, a literature survey on current MWIR detector technologies and possible QWIP material systems was conducted. Then, the fabrication and characterization of MBE-grown grating-free MWIR QWIPs using the binary InP/InAs material system on InP substrate were presented. The fabrication steps of 15 μm pitch arrays and the FPA were explained. Afterward, results of the responsivity and current measurements of the pixels were given. The fabricated QWIP had a peak responsivity of 2.7 A/W under -4.0 V bias voltage. This corresponds to a peak conversion efficiency of 61%. The peak quantum efficiency of the detectors was determined as 22%. The high conversion efficiency of the detectors shows that the low quantum efficiency and photoconductive gain disadvantages of the classical QWIP material systems can be avoided with the alternative material systems that have the ability of normal incidence radiation absorption and superior transport parameters. The expected high uniformity of the binary material system is also verified with the low (9.9%) NETD nonuniformity of the fabricated FPA.

The cut-off wavelength of the detector is much higher than 5 μm, meaning a lower dark-current activation energy. Therefore, the dark-current density of the QWIP is expected to decrease further with the adjustment of the cut-off wavelength by changing the quantum well parameters, such as the barrier/well thicknesses, and considering the effect of strain. Optimization of the quantum well doping is another option for decreasing the dark-current. The decrease in the dark-current, in return, can increase the sensor operation temperature, which is one of the main requirements of the next-generation IR photon detectors.

REFERENCES

[1] A. Rogalski, “HgCdTe infrared detector material: history, status and outlook,” *Reports on Progress in Physics*, vol. 68, no. 10, pp. 2267–2336, Oct. 2005, doi: 10.1088/0034-4885/68/10/r01

[2] A. Rogalski, “History of infrared detectors,” *Opto-Electronics Review*, vol. 20, no. 3, pp. 279–308, 2012. doi:10.2478/s11772-012-0037-7

[3] G. Ariyawansa *et al.*, “Design and modeling of InAs/GaSb Type II superlattice based dual-band infrared detectors,” *Journal of Applied Physics*, vol. 111, no. 7, p. 073107, 2012. doi:10.1063/1.3702581

[4] C. Besikci and S. V. Balci, “Diffraction-grating-free very small-pitch high-x InP/$In_xGa_{1-x}As$ quantum well infrared photodetectors,” *IEEE Electron Device Letters*, vol. 43, no. 8, pp. 1287–1290, 2022. doi:10.1109/led.2022.3185535

[5] K.-K. Choi, D. P. Forrai, D. W. Endres, and J. Sun, “Corrugated quantum-well infrared photodetector focal plane arrays,” *IEEE Journal of Quantum Electronics*, vol. 45, no. 10, pp. 1255–1264, 2009. doi:10.1109/jqe.2009.2026185

[6] K. K. Choi *et al.*, “Small pitch resonator-QWIP detectors and arrays,” *Infrared Physics & Technology*, vol. 94, pp. 118–125, 2018. doi:10.1016/j.infrared.2018.09.006

[7] A. Nedelcu, V. Guériaux, A. Berurier, N. Brière de l’Isle, and O. Huet, “Multispectral and polarimetric imaging in the LWIR: Intersubband detectors as a versatile solution,” *Infrared Physics & Technology*, vol. 59, pp. 125–132, 2013. doi:10.1016/j.infrared.2012.12.026

[8] H. Kataria *et al.*, “Novel high-resolution VGA QWIP detector,” *SPIE Proceedings*, vol. 10177, p. 101772C, May 2017. doi:10.1117/12.2267720

[9] A. Rogalski, J. Antoszewski, and L. Faraone, “Third-generation infrared photodetector arrays,” *Journal of Applied Physics*, vol. 105, no. 9, p. 091101, 2009. doi:10.1063/1.3099572

[10] A. Rogalski, P. Martyniuk, and M. Kopytko, “Challenges of small-pixel infrared detectors: a review,” *Reports on Progress in Physics*, vol. 79, no. 4, p. 046501, 2016. doi:10.1088/0034-4885/79/4/046501

[11] D. Lee *et al.*, “High-operating temperature HgCdTe: a vision for the near future,” *Journal of Electronic Materials*, vol. 45, no. 9, pp. 4587–4595, May 2016. doi:10.1007/s11664-016-4566-6

[12] L. H. Peng, J. H. Smet, T. P. Broekaert, and C. G. Fonstad, “Transverse electric and transverse magnetic polarization active intersubband transitions in narrow InGaAs quantum wells,” *Applied Physics Letters*, vol. 61, no. 17, pp. 2078–2080, 1992. doi:10.1063/1.108312

[13] G. Karunasiri *et al.*, “Normal incident InGaAs/GaAs multiple quantum well infrared detector using electron intersubband transitions,” *Applied Physics Letters*, vol. 67, no. 18, pp. 2600–2602, 1995. doi:10.1063/1.115144

[14] B. F. Levine, S. D. Gunapala, J. M. Kuo, S. S. Pei, and S. Hui, “Normal incidence hole intersubband absorption long wavelength GaAs/$Al_xGa_{1-x}As$ quantum well infrared photodetectors,” *Applied Physics Letters*, vol. 59, no. 15, pp. 1864–1866, Oct. 1991. doi:10.1063/1.106170

[15] H. S. Li, R. P. Karunasiri, Y. W. Chen, and K. L. Wang, “Electron intersubband normal incidence absorption in InGaAs/GaAs quantum wells” *Journal of Vacuum Science & Technology B: Microelectronics and Nanometer Structures Processing, Measurement, and Phenomena*, vol. 11, no. 3, pp. 922–925, May 1993. doi:10.1116/1.586740

[16] C. Besikci *et al.*, “Grating-free high-x InP/$In_xGa_{1-x}As$ mid-wavelength infrared QWIP focal plane array,” *Opto-Electronics Review*, 2023. doi:10.24425/opelre.2023.144563

[17] G. Gaussorgues, *Infrared Thermography*, Dordrecht: Springer, 2001. doi:10.1007/978-94-011-0711-2

[18] “Transmittance,” Wikipedia, https://en.wikipedia.org/wiki/Transmittance (accessed Aug. 15, 2023).

[19] A. Rogalski, “Comparison of photon and thermal detector performance,” in *Handbook of Infrared Detection Technologies*, M. Henini and M. Razeghi, Eds., Kidlington Oxford: Elsevier Advanced Technology, 2002, pp. 5–81. doi:10.1016/b978-185617388-9/50002-2

[20] P. W. Kruse, *Uncooled Thermal Imaging Arrays, Systems and Applications*, vol. TT51. Bellingham, Washington: SPIE, 2001.

[21] M. Günnar, “Characterization of molecular beam epitaxially grown CdTe layers over GaAs by spectroscopic ellipsometry,” M.S. Thesis, Izmir Institute of Technology, İzmir, 2014

[22] S. Özer, “InSb and InAsSb infrared photodiodes on alternative substrates and InP/InGaAs quantum well infrared photodetectors: pixel and focal plane array performance,” Ph.D. Thesis, Middle East Technical University, 2005.

[23] C. J. Hill *et al.*, “MBE grown type-II superlattice photodiodes for MWIR and LWIR imaging applications,” *SPIE Proceedings*, vol. 6542, p. 654205, Apr. 2007. doi:10.1117/12.721330

[24] N. Gautam *et al.*, “Three color infrared detector using InAs/GaSb superlattices with unipolar barriers,” *Applied Physics Letters*, vol. 98, no. 12, p. 121106, Mar. 2011. doi:10.1063/1.3570687

[25] J. D. Vincent, S. E. Hodges, J. Vampola, M. Stegall, and G. Pierce, *Fundamentals of Infrared and Visible Detector Operation Testing*, Second Edition. Hoboken, New Jersey: John Wiley & Sons, Inc, 2016.

[26] A. Daniels, *Field Guide to Infrared Systems*, vol. FG09. Bellingham, Washington: SPIE, 2007.

[27] H. Schneider and H. C. Liu, *Quantum Well Infrared Photodetectors: Physics and Applications*, Berlin: Springer-Verlag, 2007.

[28] O. O. Cellek, S. Memis, U. Bostanci, S. Ozer, and C. Besikci, “Gain and transient photoresponse of quantum well infrared photodetectors: A detailed ensemble Monte Carlo study,” *Physica E: Low-dimensional Systems and Nanostructures*, vol. 24, no. 3–4, pp. 318–327, 2004. doi:10.1016/j.physe.2004.06.043

[29] S. Kasap and P. Capper, *Springer Handbook of Electronic and Photonic Materials*, Second Edition. Cham, Switzerland: Springer, 2017.

[30] Y. Arslan, “Large format dual-band quantum well infrared photodetector focal plane arrays,” M.S. Thesis, Middle East Technical University, 2009.

[31] K. K. Choi, “Detection wavelength of quantum-well infrared photodetectors,” *Journal of Applied Physics*, vol. 73, no. 10, pp. 5230–5236, 1993. doi:10.1063/1.353751

[32] S. D. Gunapala, S. B. Rafol, J. K. Liu, J. M. Mumolo, and D. Z. Ting, "Thermal imaging with novel infrared focal plane arrays and quantitative analysis of thermal imagery," *Proceedings of the 2012 International Conference on Quantitative InfraRed Thermography*, 2012. doi:10.21611/qirt.2012.307

[33] M. E. Levinshtein, S. L. Rumyantsev, and M. Shur, *Ternary and Quaternary III-V Compounds*, vol. 2. Singapore: World Scientific, 1999.

[34] C. Besikci, "Nature allows high sensitivity thermal imaging with type-I quantum wells without optical couplers: a grating-free quantum well infrared photodetector with high conversion efficiency," *IEEE Journal of Quantum Electronics*, vol. 57, no. 2, pp. 1–12, 2021. doi:10.1109/jqe.2021.3052188

[35] O. O. Cellek, S. Ozer, and C. Besikci, "High responsivity InP-InGaAs quantum-well infrared photodetectors: Characteristics and focal plane array performance," *IEEE Journal of Quantum Electronics*, vol. 41, no. 7, pp. 980–985, 2005. doi:10.1109/jqe.2005.848947

[36] M. Z. Tidrow, J. C. Chiang, S. S. Li, and K. Bacher, "A high strain two-stack two-color quantum well infrared photodetector," *Applied Physics Letters*, vol. 70, no. 7, pp. 859–861, 1997. doi:10.1063/1.118298

[37] G. Hasnain, B. F. Levine, D. L. Sivco, and A. Y. Cho, "Mid-infrared detectors in the 3–5 μm band using bound to continuum state absorption in InGaAs/InAlAs multi quantum well structures," *Applied Physics Letters*, vol. 56, no. 8, pp. 770–772, 1990. doi:10.1063/1.103186

[38] A. Rogalski, "Next decade in infrared detectors," *SPIE Proceedings*, vol. 10433, p. 104330L, Oct. 2017. doi:10.1117/12.2300779

[39] Y. Arslan, T. Çolakoglu, G. Torunoglu, O. Aktas, and C. Besikci, “Enhanced performance QWIP FPAs,” *Infrared Physics & Technology*, vol. 59, pp. 108–111, 2013. doi:10.1016/j.infrared.2012.12.023

[40] J. C. James, T. L. Haran, and S. E. Lane, “Sensor performance and cut-off wavelength tradeoffs of III-V focal plane arrays,” *Opto-Electronics Review*, vol. 31, 2023. doi:10.24425/opelre.2023.144570

[41] W. E. Tennant *et al.*, “Small-pitch HgCdTe photodetectors,” *Journal of Electronic Materials*, vol. 43, no. 8, pp. 3041–3046, 2014. doi:10.1007/s11664-014-3192-4

[42] J. M. Armstrong, M. R. Skokan, M. A. Kinch, and J. D. Luttmer, “HDVIP five-micron pitch HgCdTe focal plane arrays,” *SPIE Proceedings*, vol. 9070, no. 8, pp. 907033, 2014. doi:10.1117/12.2053286

[43] “Superhawk,” Leonardo, https://electronics.leonardo.com/en/products/superhawk (accessed Aug. 15, 2023).

[44] Leo MW Product Range, https://www.lynred.com/sites/default/files/2021-07/LEO%20MW%20Datasheet.pdf (accessed Aug. 25, 2023).

[45] J. Wendler *et al.*, “New developments and state-of-the art AIM IR-modules,” *IRS^2 2009 Proceedings*, vol. Proceedings OPTO 2009 & IRS^2 2009, pp. 203–208, 2009, doi:10.5162/irs09/i1.4

[46] Y. Aytac *et al.*, “Effects of layer thickness and alloy composition on carrier lifetimes in mid-wave infrared InAs/InAsSb superlattices,” *Applied Physics Letters*, vol. 105, no. 2, p. 022107, Jul. 2014. doi:10.1063/1.4890578

[47] C. Besikci, “High-x InP/$In_xGa_{1-x}As$ quantum well infrared photodetector,” *Infrared Physics & Technology*, vol. 95, pp. 152–157, Dec. 2018. doi:10.1016/j.infrared.2018.10.018

[48] A. Rogalski, P. Martyniuk, and M. Kopytko, “Type-II superlattice photodetectors versus HgCdTe photodiodes,” *SPIE Proceedings*, vol. 11151, p. 1115114, Oct. 2019, doi:10.1117/12.2538538

[49] “Compactcore Series,” IR Cameras, https://ircameras.com/camera/compactcore/ (accessed Aug. 25, 2023).

[50] D. Z. Ting *et al.*, “InAs/InAsSb type-II strained-layer superlattice infrared photodetectors,” *Micromachines*, vol. 11, no. 11, p. 958, Oct. 2020. doi:10.3390/mi11110958

[51] R. Rehm *et al.*, “Type-II superlattices: The Fraunhofer perspective,” *SPIE Proceedings*, vol. 7660, p. 76601G, May 2010. doi:10.1117/12.850172

[52] T. L. Haran, J. C. James, and T. E. Cincotta, “Relative performance analysis of IR FPA technologies from the perspective of system level performance,” *Infrared Physics & Technology*, vol. 84, pp. 7–20, Aug. 2017. doi:10.1016/j.infrared.2017.03.007

[53] A. C. Goldberg *et al.*, “Comparison of HgCdTe and QWIP dual-band focal plane arrays,” *SPIE Proceedings*, vol. 4369, pp. 532–546, Oct. 2001. doi:10.1117/12.445313

[54] H. C. Liu, M. Buchanan, and Z. R. Wasilewski, “How good is the polarization selection rule for intersubband transitions?” *Applied Physics Letters*, vol. 72, no. 14, pp. 1682–1684, Apr. 1998. doi:10.1063/1.121151

[55] J. Hernando *et al.*, “Effect of indium content on the normal-incident photoresponse of InGaAs/GaAs quantum-well infrared photodetectors,” *Applied Physics Letters*, vol. 78, no. 16, pp. 2390–2392, Apr. 2001. doi:10.1063/1.1365951

[56] J. A. Robo *et al.*, “QWIP focal plane arrays performances from MWIR up to VLWIR,” *SPIE Proceedings*, vol. 7298, p. 72980F, May 2009. doi:10.1117/12.820470

[57] M. Sundaram *et al.*, “Multi-color IR sensors based on QWIP technology for security and surveillance applications,” *SPIE Proceedings*, vol. 6203, p. 620307, May 2006. doi:10.1117/12.673679

[58] S. D. Gunapala *et al.*, “Development of megapixel dual-band QWIP focal plane array,” *SPIE Proceedings*, vol. 6940, p. 69402T, Apr. 2008. doi:10.1117/12.783841

[59] H. Schneider *et al.*, “High-resolution 3–5 μm/8–12 μm dual-band quantum well infrared photodetector array,” *Electronics Letters*, vol. 40, no. 13, pp. 831–833, 2004. doi:10.1049/el:20040555

[60] T. Y. Wang and G. B. Stringfellow, “Strain effects on $Ga_xIn_{1-x}As$/InP single quantum wells grown by organometallic vapor-phase epitaxy with $0 \leq x \leq 1$,” *Journal of Applied Physics*, vol. 67, no. 1, pp. 344–352, Jan. 1990. doi:10.1063/1.345260

[61] R. P. Schneider and B. W. Wessels, “Optical properties of InAs/InP strained single quantum wells grown by organometallic vapor-phase epitaxy,” *Journal of Applied Physics*, vol. 70, no. 1, pp. 405–408, Jul. 1991. doi:10.1063/1.350289

[62] M. Holm, M.-E. Pistol, and C. Pryor, “Calculations of the electronic structure of strained InAs quantum dots in InP,” *Journal of Applied Physics*, vol. 92, no. 2, pp. 932–936, Jun. 2002. doi:10.1063/1.1486021

[63] P. Mohan, J. Motohisa, and T. Fukui, “Fabrication of InP/InAs/InP core-multishell heterostructure nanowires by selective area metalorganic vapor phase epitaxy,” *Applied Physics Letters*, vol. 88, no. 13, p. 133105, Mar. 2006. doi:10.1063/1.2189203

[64] B. F. Levine, “Quantum-well infrared photodetectors,” *Journal of Applied Physics*, vol. 74, no. 8, pp. R1–R81, Oct. 1993. doi:10.1063/1.354252

[65] M. Kaldirim, Y. Arslan, S. U. Eker, and C. Besikci, “Lattice-matched AlInAs-InGaAs mid-wavelength infrared QWIPs: characteristics and focal plane array performance,” *Semiconductor Science and Technology*, vol. 23, no. 8, p. 085007, 2008. doi:10.1088/0268-1242/23/8/085007

[66] Y. Arslan, S. U. Eker, M. Kaldirim, and C. Besikci, “Large format voltage tunable dual-band QWIP FPAS,” *Infrared Physics & Technology*, vol. 52, no. 6, pp. 399–402, 2009. doi:10.1016/j.infrared.2009.06.005

[67] Y. Arslan, T. Colakoglu, and C. Besikci, “Diffraction-grating-coupled high quantum efficiency InP/InGaAs quantum well infrared photodetector focal plane array,” *IEEE Journal of Quantum Electronics*, vol. 49, no. 2, pp. 186–195, 2013. doi:10.1109/jqe.2012.2237160

[68] N. Alexandru, H. Gwénaëlle, D. Adrien, M. Sylvain, and B. de Nadia, “Low pitch LWIR QWIPs: Performance level and image quality,” *Infrared Physics & Technology*, vol. 70, pp. 129–133, May 2015. doi:10.1016/j.infrared.2014.10.017

[69] H. Schneider *et al.*, “High-resolution QWIP FPAs for the 8- to 12-μm and 3- to 5-μm regimes,” *SPIE Proceedings*, vol. 4820, pp. 297–305, Jan. 2003. doi:10.1117/12.451319

[70] V. Guériaux *et al.*, “Quantum well infrared photodetectors: present and future,” *Optical Engineering*, vol. 50, no. 6, p. 061013, 2011. doi:10.1117/1.3584838

[71] S. Ozer, U. Tumkaya, and C. Besikci, “Large format AlInAs–InGaAs quantum-well infrared photodetector focal plane array for midwavelength infrared thermal imaging,” *IEEE Photonics Technology Letters*, vol. 19, no. 18, pp. 1371–1373, 2007. doi:10.1109/lpt.2007.903338

[72] S. U. Eker, Y. Arslan, M. Kaldirim, and C. Besikci, “QWIP focal plane arrays on InP substrates for single and dual-band thermal imagers,” *Infrared Physics & Technology*, vol. 52, no. 6, pp. 385–390, 2009. doi:10.1016/j.infrared.2009.05.008

[73] S. Maimon *et al.*, “Strain compensated InGaAs/InGaP quantum well infrared detector for midwavelength band detection,” *Applied Physics Letters*, vol. 73, no. 6, pp. 800–802, Aug. 1998. doi:10.1063/1.122006

[74] E. Costard *et al.*, “QWIP detectors and thermal imagers,” *Comptes Rendus Physique*, vol. 4, no. 10, pp. 1089–1102, 2003. doi:10.1016/j.crhy.2003.10.024

[75] S. D. Gunapala *et al.*, “1024 × 1024 pixel mid-wavelength and long-wavelength infrared QWIP focal plane arrays for imaging applications,” *Semiconductor Science and Technology*, vol. 20, no. 5, pp. 473–480, Mar. 2005. doi:10.1088/0268-1242/20/5/026

[76] P. Bhattacharya, S. Ghosh, and A. D. Stiff-Roberts, “Quantum dot opto-electronic devices,” *Annual Review of Materials Research*, vol. 34, no. 1, pp. 1–40, 2004. doi:10.1146/annurev.matsci.34.040203.111535

[77] Y. Reibel *et al.*, “High performance infrared fast cooled detectors for missile applications,” *SPIE Proceedings*, vol. 9819, p. 98190I, May 2016. doi:10.1117/12.2230431

[78] G. Gershon *et al.*, “10μm pitch family of InSb and XBn detectors for MWIR imaging,” *SPIE Proceedings*, vol. 10177, p. 101771I, Feb. 2017. doi:10.1117/12.2261703

[79] “FLIR A6700 MWIR,” FLIR A6700 MWIR science-grade MWIR InSb Camera | Teledyne FLIR, https://www.flir.com/products/a6700-mwir/?vertical=rd+science&segment=solutions (accessed Sep. 29, 2023).

[80] V. Donchev, J. C. Bourgoin, and P. Bois, “Dark current through GaAs/AlGaAs multiple quantum wells,” *Semiconductor Science and Technology*, vol. 17, no. 6, pp. 621–624, May 2002. doi:10.1088/0268-1242/17/6/321